J. Fluid Mech. (2020), *vol.* 897, A37. © The Author(s), 2020.
Published by Cambridge University Press
doi:10.1017/jfm.2020.388

Helicity effects on inviscid instability in Batchelor vortices

Toshihiko Hiejima†

Department of Aerospace Engineering, Osaka Prefecture University, 1-1 Gakuen-cho, Nakaku, Sakai, Osaka 599-8531, Japan

(Received 21 November 2019; revised 4 May 2020; accepted 11 May 2020)

In this paper we investigate the instability properties of Batchelor vortices with a large swirl number and a fixed axial velocity deficit. In particular, it elucidates the effect of the helicity profile on the instability of the vortices as swirling wakes. In a linear stability analysis, a negative helicity profile destabilised a vortex with a large swirl number; the name given to this instability is 'helicity instability'. Note that helicity instability is qualified for the case of axial flow with wake. In contrast, a conventional Batchelor vortex was stable at swirl numbers above a value of circulation, which is determined by the axial velocity deficit. The instability was related to a parameter D proportional to the square of the inverse azimuthal vorticity thickness. Decreasing this helicity-profile parameter increased the growth property of the vortex. Such unstable features (helicity effects) were also studied in direct numerical simulations of vortices subjected to small random disturbances at Mach numbers 2.5 and 5.0. The instability based on the vorticity thickness originally grew at the outer edge of the vortex, whereas the instability waves in a conventional Batchelor vortex originate inside the vortex core. The simulation results support the results of the linear stability analysis on the helicity profile when the parameter D is small. Because of the helicity instability, the nonlinear developments yielded a large fluctuation field with many small scales and high radial spreading rates. Even at the Mach number of 5.0, negative helicity exerted a much greater destabilisation effect than a zero entropy gradient. Therefore, the investigated novel effect established a reasonably powerful instability in compressible fluids, which is favourable for supersonic mixing.

Key words: vortex instability

1. Introduction

In many compressible or supersonic vortices and flows, instability is suppressed by compressibility effects (Bogdanoff 1983; Papamoschou & Roshko 1988; Dimotakis 1991; Clemens & Mungal 1995). Lele (1994) summarised the effects of compressibility on turbulence, and determined that naturally developing three-dimensional structures (streamwise vortical structures) enhance the growth rate of the turbulent mixing layer. Morkovin (1992) hypothesised that communication between vortical structures

† Email address for correspondence: hiejima@aero.osakafu-u.ac.jp

https://doi.org/10.1017/jfm.2020.388 Published online by Cambridge University Press

oriented perpendicular to the mainstream flow direction is uninhibited by the axial component of vorticity in streamwise vortical structures. Such structures primarily interact in the spanwise or azimuthal (non-streamwise) direction, meaning that any mixing produced by the streamwise (axial) vorticity should not be affected by compressibility. Thus, streamwise vortices in flows greatly benefit the mixing process and are structures related to vortex breakdown that is the source of large fluctuations. Indeed, at high Reynolds numbers, incompressible vortices and swirling flows with strong circulation are highly unstable and susceptible to breakdown. However, a fundamental understanding of vortex instability in compressible flows is lacking. Although a large swirl-velocity component is difficult to generate in highly supersonic flows (Wang & Sforza 1997), understanding the feature of fluctuations generated by large swirls (i.e. strong streamwise vortices) in such flows is important for improving supersonic mixing. From a convective instability perspective, the present study considers the instability properties of Batchelor vortices (Batchelor 1964), whose velocity profiles are similar to those of supersonic swirling wakes (see § 2).

The stability of Batchelor vortices in incompressible flows is commonly studied by linear stability theory. In a pioneering study, Lessen, Singh & Paillet (1974) reported that the vortices are susceptible to inviscid instabilities for all negative azimuthal wavenumbers during their temporal growth. Inviscid instability is strongest for swirl numbers $q < 1.5$ (Duck & Foster 1980). Leibovich & Stewartson (1983) demonstrated a sufficient condition for inviscid instability. Stewartson & Brown (1985), and later Heaton (2007), confirmed that inviscid vortices stabilise when $q > 2.31$. Although weak viscous unstable modes exist at all swirl numbers (Lessen & Paillet 1974; Khorrami 1991; Mayer & Powell 1992; Fabre & Jacquin 2004), they are much smaller than strong inviscid modes. From a spatial growth perspective, Parras & Fernandez-Feria (2007) considered viscous unstable modes at high swirl numbers ($q > 1.5$) and large Reynolds numbers ($Re > 10^3$). Delbende, Chomaz & Huerre (1998) and Olendraru *et al.* (1999) investigated absolute and convective instabilities in Batchelor vortices. The classical stability of an incompressible Batchelor vortex was summarised by Green (1995) and Alekseenko, Kuibin & Okulov (2007).

Viscous instabilities and transient growths of Batchelor vortices with large q have also been studied. Transient growth is detailed in Schmid & Henningson (2001). The analysis of transient growth involves solution of the initial value problem for small amplitude disturbances to a given base flow. Heaton & Peake (2006) showed that in the inviscid state, Batchelor vortices are susceptible to algebraic and transient growth at all swirl levels. Later, they studied transient growth in the large q regime (Heaton & Peake 2007).

Ragab & Sreedhar (1995), Delbende & Rossi (2005), Abid (2008), Duraisamy & Lele (2008) and Di Pierro & Abid (2011) have studied periodic temporal development during the nonlinear evolution of incompressible Batchelor vortices in disturbances. Abid (2008) considered nonlinear mode selection in incompressible Batchelor vortices and showed that a hypothesis, which the linear unstable mode comes to the global mode, is violated near the flow axis, whereas far from the vortex axis, the nonlinear evolution favours the linear unstable mode at large swirl numbers. The spatial development of Batchelor vortices was studied by Broadhurst & Sherwin (2008), Mao & Sherwin (2012) and Viola, Arratia & Gallaire (2016). When perturbed by the optimal disturbance, vortex growth vibrates under a transient-energy growth mechanism (Mao & Sherwin 2012). In a global analysis of non-parallel flows, Heaton, Nichols & Schmid (2009) found the correspondence between global modes and local absolute modes. Viola *et al.* (2016) investigated mode selection in a non-parallel

https://doi.org/10.1017/jfm.2020.388 Published online by Cambridge University Press

spatially developing Batchelor vortex subjected to forcing frequencies. They showed that the mode selection mechanism is connected to the local stability properties of the flow.

In contrast to incompressible flows, compressible Batchelor vortices have been rarely investigated. Inviscid linear stability analyses by Stott & Duck (1994) and Hiejima (2013) showed that vortex instabilities are suppressed at high Mach numbers. Khorrami & Chang (1997) studied the linear and nonlinear evolution of small disturbances in supersonic streamwise vortices, applying local linear stability analysis and parabolised stability equations, respectively. They found that nonlinear effects tend to stabilise the vortex by increasing the downstream swirl intensity. The growth of the modes was assessed as convectively unstable. Instabilities with density variations have been studied under incompressible conditions, but not in compressible flows. Sipp *et al.* (2005), Joly, Fontane & Chassaing (2005) and Di Pierro & Abid (2012) have considered Batchelor vortices with variable densities. The patterns of vortex evolution in these studies differed considerably from those of a conventional Batchelor vortex. Thereby, unstable mechanisms based on density variations have been attributed to entropy instabilities (Hiejima 2014) such as the Rayleigh–Taylor instability.

Moffatt & Tsinober (1992) linked the qualitative changes in flow topology resulting from vortex breakdown to large changes in helicity. They considered that vortex flows can be characterised and classified by the helicity density. Moffatt (2017) also stated that total helicity is important for turbulent thermal convection in a strongly rotating fluid, and is invariant even in a viscous fluid. Pouquet & Mininni (2010) showed that small-scale structures and their intermittency properties depend on the presence or absence of helicity in rotating flows. Holm & Kerr (2007) indicated a central role of helicity in the dynamical evolution of vortex structures; in particular, the global helicity can change only through the dissipation of oppositely signed helicities. In turbulent systems, energy is transferred to modes with opposite helicity (Sahoo, Bonaccorso & Biferale 2015). These results demonstrate that vortical topology changes rely on vortex structures of oppositely signed helicity. In previous studies at small q (Hiejima 2015*a*), the profiles of a Batchelor vortex with negative helicity were associated with a large azimuthal vorticity thickness, leading to highly destabilized vortices in the flows. Although helicity is a major effecter of evolving vortex structures, the effect of helicity instability at large q has not been clarified.

The present study analyses helicity-unstable effects in a Batchelor vortex with a large swirl number. The stabilisation mechanism of inviscid modes remains largely unknown at large swirl numbers. From a stability analysis perspective, both the linear growth properties and the nonlinear developments are important. In classical studies of inviscid instabilities, the linear stability analyses and direct numerical simulations of the vortices are conducted for varying values of the helicity-profile parameter, which is based on the azimuthal vorticity thickness. To resolve the difficult supersonic-mixing problem, we must extract the potential instability-inducing capacity of helicity, which has not been previously reported.

The remainder of this paper is organised as follows. In § 2 the base flow in compressible Batchelor vortices is described. In § 3 the linear stability analysis of the Batchelor vortices with large swirls is formulated and the stability results are focused on helicity instability. In § 4 the method and computational conditions of the direct numerical simulations are described. In § 5 the results of spatial development related to helicity instability are provided and discussed. For varying azimuthal vorticity thickness of the base flow, this section clarifies the effects of Batchelor vortices with a large swirl number on the helicity instability in numerical simulations. Conclusions are presented in § 6.

https://doi.org/10.1017/jfm.2020.388 Published online by Cambridge University Press

2. Compressible Batchelor vortices

Batchelor vortices (Batchelor 1964) are adopted as the base flow in stability analyses of compressible streamwise vortices, because their velocity profiles are compatible with those of experimental supersonic swirling wakes at high Reynolds numbers (Cattafesta & Settles 1992; Naughton, Cattafesta & Settles 1997; Wang & Sforza 1997; Kalkhoran, Smart & Wang 1998). The three velocity components (radial, azimuthal and streamwise), density, pressure, temperature and entropy are expressed in cylindrical polar coordinates (r^*, θ^*, x^*) as u_r^*, u_θ^*, u_x^*, ρ^*, p^*, T^* and s^*, respectively (note that dimensional quantities are superscripted with asterisks). The axial vorticity ω_x^*, axial velocity u_x^* and radial velocity u_r^* are respectively given by

$$\omega_x^*(r^*) = \omega_{max}^* \mathrm{e}^{-C_1 r^{*2}}, \tag{2.1}$$

$$u_x^*(r^*) = U_\infty^* - \Delta U_x^* \mathrm{e}^{-C_2 r^{*2}}, \tag{2.2}$$

$$u_r^*(r^*) \simeq 0, \tag{2.3}$$

where ω_{max}^* denotes the maximum axial vorticity, U_∞^* is the free stream velocity and ΔU_x^* is the axial velocity deficit. Denote by C_1 and C_2 the profile constants. The vortex radius is quantified by the swirl scale δ_s^* and the thickness $\delta_{\omega_\theta}^*$ of the azimuthal vorticity, which are respectively defined as

$$\delta_s^* = \sqrt{\frac{\Gamma^*}{\pi \omega_{max}^*}} = \frac{1}{\sqrt{C_1}}, \quad \delta_{\omega\theta}^* = \frac{u_x^*(\infty) - u_x^*(0)}{\left.\dfrac{\partial u_x^*}{\partial r}\right|_{max}} = \sqrt{\frac{e}{2C_2}}, \tag{2.4a,b}$$

where Γ^* represents the total circulation of the entire distributed axial vorticity. The free stream Mach number M_∞ and Reynolds number Re are respectively given by

$$M_\infty = \frac{U_\infty^*}{\sqrt{\gamma R^* T_\infty^*}}, \quad Re = \frac{\rho_\infty^* U_\infty^* \delta_s^*}{\eta_\infty^*}. \tag{2.5a,b}$$

Here, T_∞^* is the free stream temperature, R^* is the gas constant, γ is the ratio of specific heats and η_∞^* is the viscosity. The entropy profile s^* that governs the thermodynamic profile is denoted by

$$\Delta s^* = s^* - s_0^* = C_v^* \log_e \frac{p^*}{\rho^{*\gamma}}, \tag{2.6}$$

where Δs^* is the entropy variation, s_0^* is a constant and C_v^* represents the specific heat at constant volume.

After normalising by the reference length δ_s^* of a compressible Batchelor vortex, the free stream velocity U_∞^* and the density ρ_∞^*, the physical variables become

$$\left.\begin{gathered} \rho = \frac{\rho^*}{\rho_\infty^*}, \quad u_r = \frac{u_r^*}{U_\infty^*}, \quad u_\theta = \frac{u_\theta^*}{U_\infty^*}, \quad u_x = \frac{u_x^*}{U_\infty^*}, \quad p = \frac{p^*}{\rho_\infty^* U_\infty^{*2}}, \\ T = \frac{R^*}{U_\infty^{*\,2}} T^*, \quad s = \frac{s^*}{C_v^*}, \quad r = \frac{r^*}{\delta_s^*}, \quad x = \frac{x^*}{\delta_s^*}, \quad t = \frac{U_\infty^*}{\delta_s^*} t^*. \end{gathered}\right\} \tag{2.7}$$

The azimuthal velocity u_θ is obtained by integrating the axial vorticity (2.1), and the axial velocity u_x and radial velocity u_r are respectively derived from (2.2) and (2.3):

$$u_r(r) = 0, \quad u_\theta(r) = \frac{q}{r}(1 - \mathrm{e}^{-r^2}), \quad u_x(r) = 1 - \mu \mathrm{e}^{-Dr^2}. \tag{2.8a–c}$$

https://doi.org/10.1017/jfm.2020.388 Published online by Cambridge University Press

Here

$$q=\frac{\Gamma^*}{2\pi U_\infty^* \delta_s^*},\quad \mu=\frac{\Delta U_x^*}{U_\infty^*},\quad D=\frac{C_2}{C_1}=\frac{e}{2}\left(\frac{\delta_s^*}{\delta_{\omega\theta}^*}\right)^2, \tag{2.9a–c}$$

where q and $\mu\,(\leqslant 1)$ represent the circulation (or swirl number) and the velocity deficit, respectively. The parameter $D\,(>0)$, which is proportional to the square of the inverse azimuthal vorticity thickness, is a major influencer of helicity instability (Hiejima 2015*a*). When D is sufficiently large, the thickness $\delta_{\omega\theta}^*$ becomes smaller and the vortex flow comes close to the Lamb–Oseen vortex while the instability should be close to that of the axial wake in a rotating frame. In contrast, when D is sufficiently small, the $\delta_{\omega\theta}^*$ becomes larger and the vortex flow comes close to a developed wake without swirl. The features of these base flows based on the limit values of D are useful in understanding the instabilities.

Thermodynamic profiles in a compressible Batchelor vortex are poorly understood because their measurements are rare. The base flows can be reasonably assumed as inviscid supersonic flows because the Reynolds numbers are sufficiently large under supersonic conditions and stability analyses assume laminar flows. The normalised equation of state is $p=\rho T$. In a perfect gas with simple molecules, the specific heat is constant over a wide temperature range under Mach numbers below hypersonic flows. The local speed of sound c is then defined as

$$c=\sqrt{\gamma\frac{p}{\rho}}. \tag{2.10}$$

The entropy gradient is described by the Crocco equation:

$$\frac{1}{\gamma-1}T\frac{\mathrm{d}s}{\mathrm{d}r}=\frac{\gamma}{\gamma-1}\frac{\mathrm{d}T_0}{\mathrm{d}r}-u_\theta\omega_x+u_x\omega_\theta. \tag{2.11}$$

Here ω_x and ω_θ are the axial and azimuthal vorticities, respectively. Experiments have shown that the stagnation temperature T_0 is approximately uniform (Cattafesta & Settles 1992). This assumption reasonably holds for the linear instability property behind developed flows. In this study, $\mathrm{d}s/\mathrm{d}r$ was derived by setting $\mathrm{d}T_0/\mathrm{d}r=0$ in (2.11). Using the radial momentum equation and the derivation of the entropy definition in (2.6), we relate the density ρ to the pressure p as follows:

$$\frac{\mathrm{d}p}{\mathrm{d}r}=\rho\frac{{u_\theta}^2}{r},\quad \frac{\mathrm{d}\rho}{\mathrm{d}r}=\frac{\rho}{\gamma}\left(\frac{1}{p}\frac{\mathrm{d}p}{\mathrm{d}r}-\frac{\mathrm{d}s}{\mathrm{d}r}\right). \tag{2.12a,b}$$

Equations (2.11) and (2.12) give the density and pressure profiles in a basic inviscid steady flow.

3. Linear stability analysis

3.1. *Asymptotic analysis*

The inviscid linear stability of Batchelor vortices is analysed in cylindrical polar coordinates. Each flow variable is assumed to consist of its mean part ($\overline{\ }$) and a small amplitude disturbance ($\widetilde{\ }$). These flow variables are written as

$$\begin{Bmatrix}\rho(r,\theta,x,t)\\ u_r(r,\theta,x,t)\\ u_\theta(r,\theta,x,t)\\ u_x(r,\theta,x,t)\\ p(r,\theta,x,t)\end{Bmatrix}=\begin{Bmatrix}\overline{\rho}(r)\\ \overline{u}_r(r)\\ \overline{u}_\theta(r)\\ \overline{u}_x(r)\\ \overline{p}(r)\end{Bmatrix}+\begin{Bmatrix}\widetilde{\rho}(r,\theta,x,t)\\ \widetilde{u}_r(r,\theta,x,t)\\ \widetilde{u}_\theta(r,\theta,x,t)\\ \widetilde{u}_x(r,\theta,x,t)\\ \widetilde{p}(r,\theta,x,t)\end{Bmatrix}. \tag{3.1}$$

https://doi.org/10.1017/jfm.2020.388 Published online by Cambridge University Press

In terms of the normal modes, the linear disturbances are expressed as

$$\{\widetilde{\rho}, \widetilde{u}_r, \widetilde{u}_\theta, \widetilde{u}_x, \widetilde{p}\} = \{R(r), U(r), V(r), W(r), P(r)\} \exp[\boldsymbol{i}(\alpha x + m\theta - \omega t)], \tag{3.2}$$

where m is the azimuthal wavenumber (integer), α is the axial wavenumber (real) and $\omega = \omega_r + \boldsymbol{i}\,\omega_i$ (complex), where ω_r is the angular frequency and ω_i is the temporal growth rate. The inviscid linearized disturbance equations are written as

$$\frac{\mathrm{d}P}{\mathrm{d}r} = A(r)P + B(r)U, \quad \frac{\mathrm{d}U}{\mathrm{d}r} = C(r)P + D(r)U, \tag{3.3a,b}$$

$$\left.\begin{aligned} A(r) &= \frac{\overline{u}_\theta{}^2}{r\overline{c}^2} - \frac{2m\overline{u}_\theta}{r^2\overline{\phi}}, \quad B(r) = \frac{\boldsymbol{i}\overline{\rho}}{\overline{\phi}}\left(N^2 + \frac{2\overline{u}_\theta\overline{\omega}_x}{r} - \overline{\phi}^2\right), \\ C(r) &= \frac{\boldsymbol{i}}{\overline{\rho}\overline{\phi}}\left(\alpha^2 + \frac{m^2}{r^2} - \frac{\overline{\phi}^2}{\overline{c}^2}\right), \quad D(r) = \frac{1}{\overline{\phi}}\left(\frac{m}{r}\overline{\omega}_x - \alpha\overline{\omega}_\theta\right) - \frac{\overline{u}_\theta{}^2}{r\overline{c}^2} - \frac{1}{r}, \end{aligned}\right\} \tag{3.4}$$

where

$$\overline{\phi} = -\omega + m\frac{\overline{u}_\theta}{r} + \alpha\overline{u}_x, \quad N^2 = -\frac{\overline{u}_\theta{}^2}{\gamma r}\frac{\mathrm{d}\overline{s}}{\mathrm{d}r}, \quad \overline{\omega}_x = \frac{\mathrm{d}\overline{u}_\theta}{\mathrm{d}r} + \frac{\overline{u}_\theta}{r}, \quad \overline{\omega}_\theta = -\frac{\mathrm{d}\overline{u}_x}{\mathrm{d}r}. \tag{3.5a–d}$$

Here, $\overline{\phi}$ is the Doppler frequency and N is the Brunt–Väisälä frequency.

Introducing a small parameter ε $(0 < \varepsilon \ll 1)$ to define the rescaled wavenumbers; $\tilde{m} = \varepsilon m$, $\tilde{\alpha} = \varepsilon\alpha$ (Leblanc & Le Duc 2005; Di Pierro & Abid 2010) and obtaining $\omega \simeq \Delta/\varepsilon + \boldsymbol{i}\chi$ as the asymptotic solution of (3.3) at large wavenumbers ($|m| \gg 1$, $|\alpha| \gg 1$), we can estimate the temporal growth rate χ whose modes are part of a continuum spectrum. In compressible swirling flows, Hiejima (2015*b*) determined the squared growth rate χ^2 as

$$\chi^2(r) = \chi_{\mathrm{I}}^2 + \chi_{\mathrm{II}}^2 + \chi_{\mathrm{III}}^2 + \chi_{\mathrm{IV}}^2, \tag{3.6}$$

$$\chi_{\mathrm{I}}^2 = -N^2, \tag{3.7}$$

$$\chi_{\mathrm{II}}^2 = \Upsilon(r)\frac{r}{\tilde{\alpha}}\left[\left(\overline{\mathscr{U}}_i \times \widetilde{\mathscr{K}_i}\right)\cdot\overline{\omega}_x\right], \tag{3.8}$$

$$\chi_{\mathrm{III}}^2 = \Upsilon(r)\left(\frac{\tilde{m}}{\tilde{\alpha}}\right)(-\overline{h}), \tag{3.9}$$

$$\chi_{\mathrm{IV}}^2 = \frac{2\left(\dfrac{c_{ph}}{\overline{c}}\right)^2}{1 - \left(\dfrac{c_{ph}}{\overline{c}}\right)^2}\frac{\overline{M}_\theta}{r}\overline{c\omega}_x, \tag{3.10}$$

where

$$\Delta = \tilde{m}\frac{\overline{u}_\theta}{r} + \tilde{\alpha}\overline{u}_x, \quad \overline{M}_\theta = \frac{\overline{u}_\theta}{\overline{c}}, \quad c_{ph} = \frac{\omega_r}{\sqrt{\alpha^2 + \left(\dfrac{m}{r}\right)^2}} \simeq \frac{\Delta}{\sqrt{\tilde{\alpha}^2 + \left(\dfrac{\tilde{m}}{r}\right)^2}}, \tag{3.11a–c}$$

$$\Upsilon(r) = \frac{2}{\left[r^2 + \left(\dfrac{\tilde{m}}{\tilde{\alpha}}\right)^2\right]\left[1 - \left(\dfrac{c_{ph}}{\overline{c}}\right)^2\right]}. \tag{3.12}$$

https://doi.org/10.1017/jfm.2020.388 Published online by Cambridge University Press

We define the vector of velocity $\overline{\mathscr{U}}_i$ and the vector of disturbance wavenumbers $\widetilde{\mathscr{K}_i}$ as

$$\overline{\mathscr{U}}_i = \begin{pmatrix} \overline{u}_x \\ \overline{u}_\theta \end{pmatrix} \quad \widetilde{\mathscr{K}_i} = \begin{pmatrix} \tilde{\alpha} \\ \tilde{m}/r \end{pmatrix}. \tag{3.13a,b}$$

The term II in (3.6) is expressed as the variable depending on the cross product of the two vectors. In addition, the vorticity vector $\overline{\mathscr{W}}_i$ is defined as

$$\overline{\mathscr{W}}_i = \begin{pmatrix} \overline{\omega}_x \\ \overline{\omega}_\theta \end{pmatrix}. \tag{3.14}$$

The term III in (3.6) includes the helicity density $\overline{h}$, given by

$$\overline{h} = \overline{\mathscr{U}}_i \, \overline{\mathscr{W}}_i. \tag{3.15}$$

Moreover, $\omega_r \simeq \Delta/\varepsilon$ denotes the angular frequency and the term IV in (3.6) is related to Δ, which can be rewritten as

$$\Delta = \overline{\mathscr{U}}_i \, \overline{\mathscr{K}}_i. \tag{3.16}$$

Furthermore, taking the derivative of Δ in (3.11), we derive the relation

$$\Delta' + \frac{2\,\tilde{m}\,\overline{u}_\theta}{r^2} = \overline{\mathscr{W}}_i \times \widetilde{\mathscr{K}_i}, \tag{3.17}$$

where the prime denotes differentiation with respect to r. Thus, the three vectors influence each other on stability conditions.

The terms in (3.6) describe four types of destabilizing elements in swirling wake flows. Term I expresses the entropy gradient related to compressibility effects (Hiejima 2019). Note that when the stagnation temperature is uniform in the thermodynamic profile, χ_{I}^2 can be rewritten as

$$\chi_{\mathrm{I}}^2 = -\frac{\overline{M}_\theta}{r}\left(\overline{\mathscr{U}}_i \times \overline{\mathscr{W}}_i\right). \tag{3.18}$$

Here, we have used (2.11), (3.5) and (3.11). Equation (3.18) indicates that when q is large, the vortex becomes stabilised because term I becomes large and negative. Term II includes the sources of helical-shear effects that occur in the vortex core, i.e. the spiral instability. Term III describes the negative helicity density on the swirling wake flows. Defining the angle between $\overline{\mathscr{U}}_i$ and $\overline{\mathscr{W}}_i$ as ψ, the instability caused by this term (the name 'helicity instability') exists over $\pi/2 < \psi < 3/2\pi$ if the angle is a blunt angle. Note that helicity instability is qualified for the case of axial flow with wake. Term IV includes the phase velocity c_{ph} and the local speed of sound $\overline{c}$, which are related to the acoustic unstable wave, and is very weak in wake-type flows. Evidently, term I is determined only by the velocity profiles in the base flow, while terms II, III and IV are included in the disturbance wavenumbers. The growth rate of the asymptotic analysis is thus obtained from (3.6), but $(\tilde{m}/\tilde{\alpha})$ is unknown.

Eckhoff & Storesletten (1978) and Leblanc & Le Duc (2005) assumed that, for some r_0 in compressible swirling flows,

$$\Delta'(r_0) = 0. \tag{3.19}$$

https://doi.org/10.1017/jfm.2020.388 Published online by Cambridge University Press

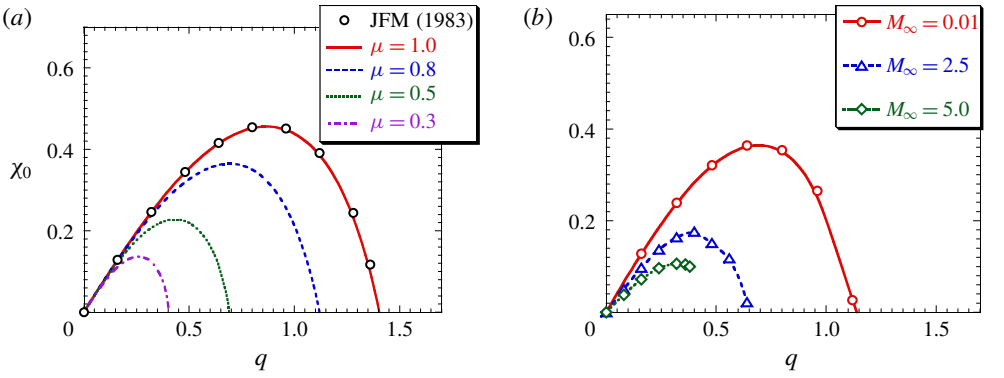


FIGURE 1. Temporal growth rates χ_0 in (3.6) as functions of circulation q for $D = 1.0$: (*a*) various μ at $M_\infty = 0.01$; ○, the growth rate obtained from the formula given by Leibovich & Stewartson (1983); (*b*) three Mach numbers M_∞ at $\mu = 0.8$.

From (3.19), $(\tilde{m}/\tilde{\alpha})$ is obtained. In compressible cases, the two conditions (3.6) and (3.19) are comparable to those of incompressible homogenous flows found by Leibovich & Stewartson (1983). Therefore, $\chi_0 = \sqrt{\chi^2(r_0)}$ is uniquely determined from the base flows alone.

Although the Lamb–Oseen vortex is always stable, the Batchelor vortex becomes unstable depending on the axial velocity deficit in incompressible flows (Alekseenko *et al.* 2007). To verify the effect of the axial velocity deficit in conventional Batchelor vortices ($D = 1.0$ and $M_\infty = 0.01$), the relations between the growth rate χ_0 in (3.6) and the swirl number q at deficit μ are shown in figure 1(*a*). When $\mu = 1.0$, the maximum q approximated $\sqrt{2}$, consistent with the very strong inviscid mode of the incompressible Batchelor vortex for $q < 1.5$ (Heaton & Peake 2007). The growth rates χ_0 were also in good agreement with that of Leibovich & Stewartson (1983). Note that the asymptotic growth rate of Billant & Gallaire (2013) is more accurate than that of Leibovich & Stewartson (1983) over a wider range of axial wavenumbers in the Batchelor vortex. The growth rate and existence range of the unstable mode decreased with decreasing deficit μ. The μ exerted a large effect on growth rate, as evidenced by dividing the growth rate χ_0 for $\mu = 0.3$ by that for $\mu = 1.0$. To understand the effect of the Mach number M_∞ on the growth rate χ_0, we plotted the relations between the growth rate χ_0 and the circulation q for three Mach numbers at $\mu = 0.8$ (see figure 1*b*). Both χ_0 and q at the maximum growth rate decreased with increasing M_∞. For instance, the maximum growth rate was smaller at $M_\infty = 2.5$ and $\mu = 0.8$ than at $M_\infty = 0.01$ and $\mu = 0.8$, and corresponded to that between $\mu = 0.3$ and 0.5 at $M_\infty = 0.01$. In figure 1(*b*), note the end point of the line at $M_\infty = 5.0$. This point marks the limit of q because the static pressure at the vortex centre of a compressible flow must be positive.

3.2. *Helicity instability in the case of axial flow with wake*

Figure 2 plots the temporal growth rate χ_0 in (3.6) as a function D for $\mu = 0.8$ at $M_\infty = 0.01$, 1.0, 2.5 and 5.0. Note that when $D = 0$, the vortex (2.8) corresponds to the Lamb–Oseen vortex (stable vortex). When $M_\infty = 0.01$, the effect of D on small q is weak. As q increases, the χ_0 divides dichotomously. Note that the vortex with large q is stable at $D = 1.0$, while it becomes unstable with decreasing and increasing D. The results are important in that the stability characteristic has not been investigated in a conventional Batchelor vortex. Although the growth rate of the vortex with large

https://doi.org/10.1017/jfm.2020.388 Published online by Cambridge University Press

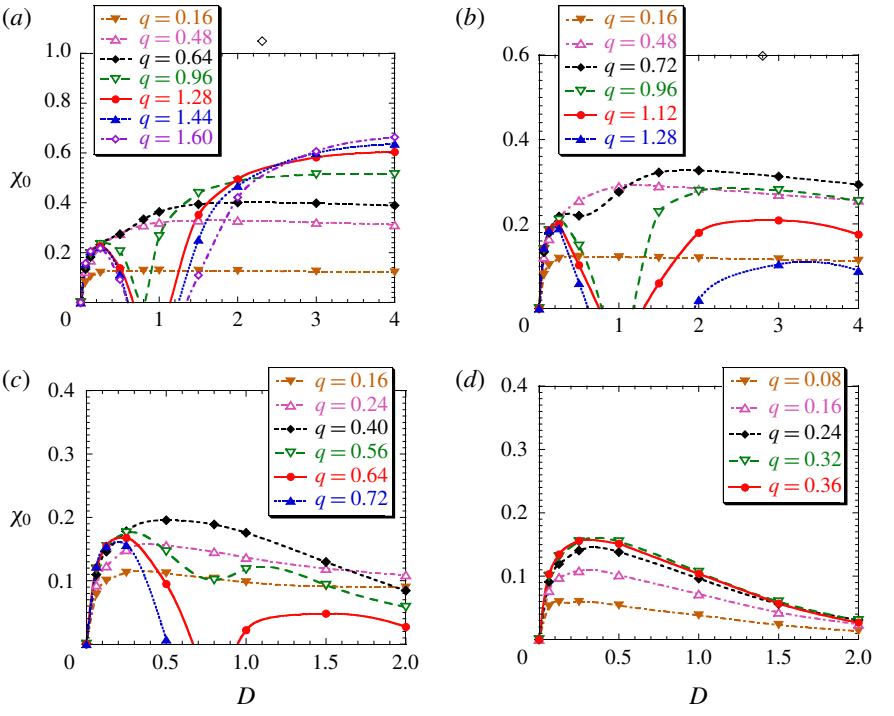


FIGURE 2. Temporal growth rates χ_0 as functions of the parameter D in the asymptotic analysis (3.6) for various q and $\mu = 0.8$: (*a*) $M_\infty = 0.01$, (*b*) $M_\infty = 1.0$, (*c*) $M_\infty = 2.5$ and (*d*) $M_\infty = 5.0$.

q divides between $D < 1.0$ and $D > 1.0$ even at $M_\infty = 1.0$, it decreases at $D > 1.0$ in contrast to the case of $M_\infty = 0.01$. When $M_\infty = 2.5$ and $D = 1.0$, the growth rate was very small at $q = 0.64$, and was not observed at $q = 0.72$, consistent with the results of figure 1(*b*). Interestingly, when q was large, the growth rate χ_0 rose with decreasing D and the vortices become unstable. When $M_\infty = 5.0$, all χ_0–D curves exhibited a similar feature, that is, the maximum growth rate χ_0 for each q occurred at small D; moreover, the maximum growth rates at $M_\infty = 2.5$ and 5.0 were quantitatively similar. In previous works (Hiejima 2014, 2019), the Mach-number-dependent stabilisation effect was attributed to term I in the entropy profile. However, the present result suggests that some other factor associated with the small D explains the destabilisation effect. Elucidating this factor would be helpful for defeating the compressible effects.

Figure 3 plots the helicity density profiled $\overline{h}$ calculated by (3.15) for various D at $q = 0.64$ and $\mu = 0.8$. Note that the figure does not depend on the magnitude of q and the helicity density profile varies on the parameter D. According to term III in (3.9), the vortex becomes unstable when the helicity becomes negative (i.e. $\overline{h} < 0$) under the axial velocity profiles without reverse flow: $0 < \mu \leqslant 1$. Because helicity instability is expressed as term III > 0, the degree of helicity instability increases as D reduces. In the case of $D = 0.25$, the helicity presented a local minimum at $r = 1.85$; this condition is the most effective condition for helicity instability.

Why does a Batchelor vortex with large q stabilise? The mechanism of this phenomenon has not been clarified. As shown in figure 2, the vortices with large q were excitedly destabilised by the parameter D, which is related to helicity instability on the condition of $0 < \mu \leqslant 1$. Previously, terms II and III in (3.6) were considered together, but their individual analyses provide glimpses into new unstable structures

https://doi.org/10.1017/jfm.2020.388 Published online by Cambridge University Press

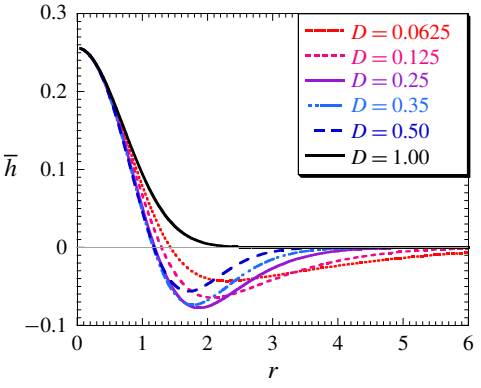


FIGURE 3. Helicity density profiles $\overline{h}$ for various D at $q = 0.64$ and $\mu = 0.8$.

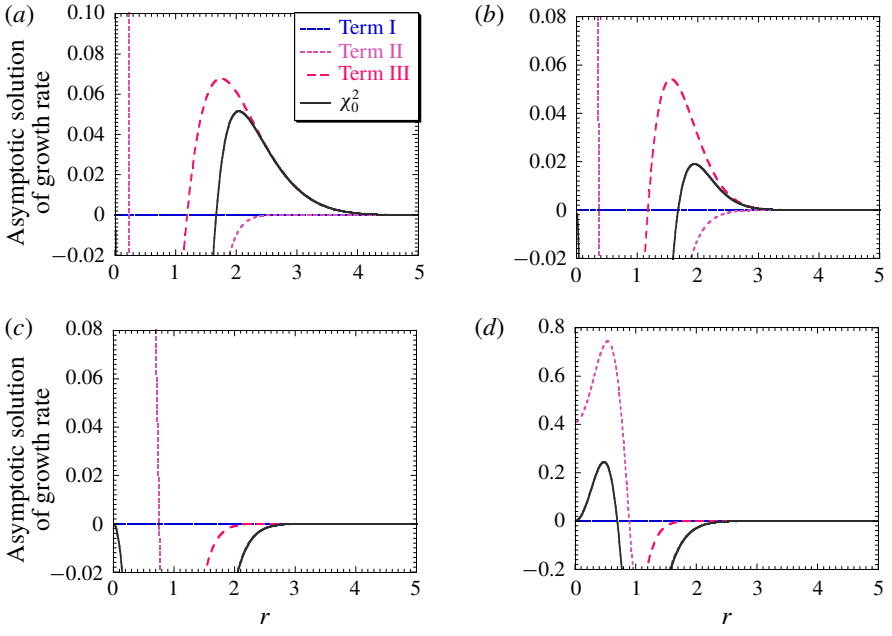


FIGURE 4. Profiles of squared temporal growth rates χ_0^2 for each term in (3.6), obtained for a Batchelor vortex with $q = 1.28$ and $\mu = 0.8$ at $M_\infty = 0.01$: (*a*) $D = 0.25$, (*b*) $D = 0.50$, (*c*) $D = 1.0$ and (*d*) $D = 2.0$.

in swirling wake flows. In term II, enlarging q also enlarges $-\overline{u}_\theta$ and stabilises the vortex because $\chi_{\mathrm{II}}^2 \propto (\tilde{m}/\tilde{\alpha})(\overline{u}_x/r) - \overline{u}_\theta$. In term III, enlarging D stabilises the vortex because $-\overline{h} < 0$.

To clarify the dominant instability property, figures 4 and 5 show the distributions of the squared growth rate χ_0^2 of terms I–III in (3.6) for various D. For an incompressible vortex with $q = 1.28$ and $\mu = 0.8$, the effect of D on growth rate is shown in figure 4. In all cases, term I was almost nothing because $M_\infty = 0.01$. When D was small, the helicity instability that was caused by term III was strong. When $D = 1.0$, the vortex was stable and when $D = 2.0$, the strong unstable due to term II occurred in the vortex core. Note that the feature is close to that of a conventional Batchelor vortex.

https://doi.org/10.1017/jfm.2020.388 Published online by Cambridge University Press

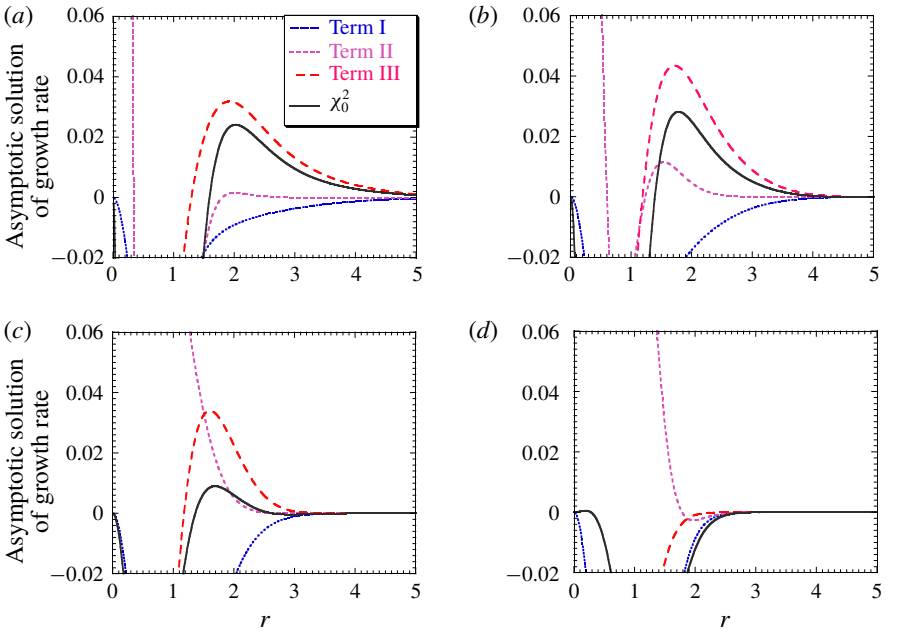


FIGURE 5. Profiles of squared temporal growth rates χ_0^2 for each term in (3.6), obtained for a Batchelor vortex with $q = 0.64$ and $\mu = 0.8$ at $M_\infty = 2.5$: (*a*) $D = 0.125$, (*b*) $D = 0.25$, (*c*) $D = 0.50$ and (*d*) $D = 1.0$.

The effect of term II decreases as the Mach number increases (see figure 2). In the vicinity of $D = 1.0$, the parameter D changes an instability effect from helicity instability (term III) to spiral instability (term II). The results definitely demonstrate the significance of separating terms II and III in (3.6). In figure 5 the parameters were fixed as $M_\infty = 2.5$, $q = 0.64$ and $\mu = 0.8$ in varying D. In all cases, term I went negative because $M_\infty = 2.5$. Term II made a slight contribution around $r = 1.5$ only when $D = 0.25$. When D was 0.125, 0.25 and 0.50, the helicity effect was large because χ_0^2 was largely contributed by term III. As seen in (3.18), the stabilisation effect of term I was high at large q, but was largely surpassed by the unstable effect of term III, as shown by $\chi_0 > 0$. As the parameter D decreased, the impacted area spread in the radial direction and the growth rate in all cases was large outside the vortex core. The extension of the instability region beyond the vortex core is likely to be an important feature as will be describe later. When $D = 1.0$, term III almost vanished. In conventional Batchelor vortices ($D = 1.0$) with high swirl intensity q, the helicity profile participates in the stabilisation. The mechanism is clearly explained by the helicity effect (term III). Therefore, the asymptotic solution distributions in these figures show the features of helicity instability. Further analysis will investigate the instability caused by term III, which relates to the helicity profile. Based on the perspective that the uniform axial velocity component U_∞^* in (2.2) should not matter in temporal stability, the case of axial flow with jet is described in appendix A.

3.3. *Temporal and spatial growth rates*

Applying linear stability theory, this subsection describes a classical convectively unstable feature of a Batchelor vortex with large q. The eigenvalues and eigenfunctions of the inviscid linearized disturbance equations (3.3) were solved by a shooting method.

https://doi.org/10.1017/jfm.2020.388 Published online by Cambridge University Press

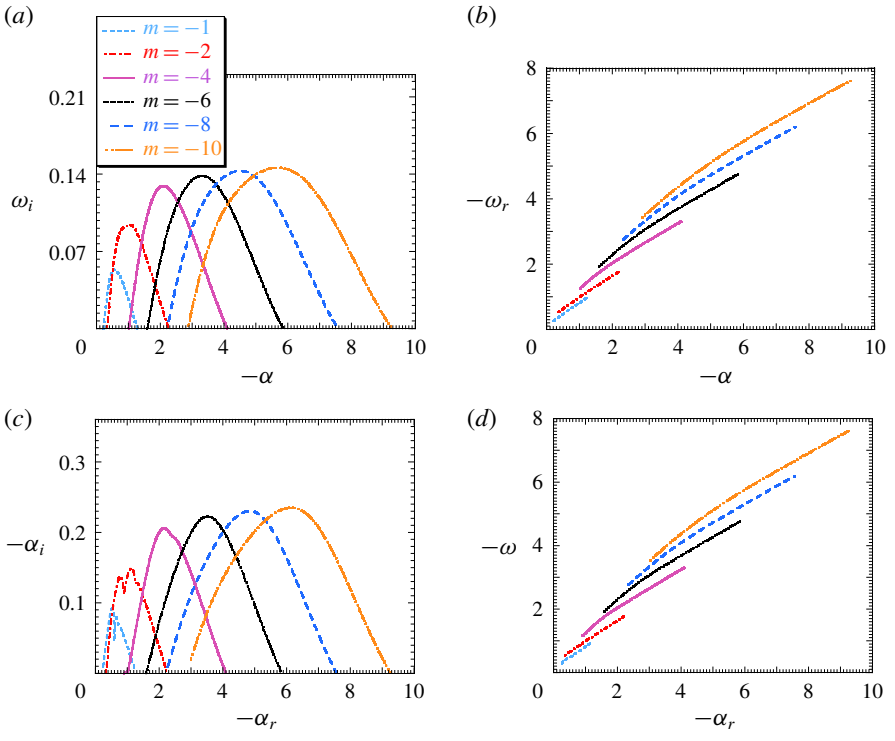


FIGURE 6. Growth rate (a,c) and frequency (b,d) as functions of axial wavenumber for $q = 0.64$, $\mu = 0.8$ and $D = 0.25$ at $M_\infty = 2.5$: (a,b) temporal growth and (c,d) spatial growth.

The solution is detailed in the reference (Hiejima 2013). Increasing the parameter D decreased the growth rate and narrowed the band (data not shown). All modes of $D = 1.0$ were stable owing to their small growth rates in the stability analysis. Based on the results of figure 5, the helicity effects were investigated at $D = 0.25$, $M_\infty = 2.5$, $q = 0.64$ and $\mu = 0.8$.

First, consider the temporal evolution of the vortex. Figure 6(a,b) plots the growth rate ω_i and frequency ω_r as functions of axial wavenumber α. As the q was relatively large, the modes of the low azimuthal wavenumbers were weak. However, the growth rate increased with increasing m and the band of the unstable mode broadened. Part of the phase velocities ω_r/α were nearly identical without depending on m. Here, it is important to compare the present result with the asymptotic analysis (3.6). The ratio of the maximum growth rates $\omega_i/\chi_0 = 0.86$ at $m = -10$ and the χ_0 overestimates the growth rate, similar to the results of Hiejima (2015*b*). Note that (3.17) satisfies (3.19) when q is small (spiral instability) or r_0 is large (helicity instability). The present discrepancy possibly arises through the moderate wavenumber, not be enough as an asymptotic solution of (3.3) at large wavenumbers.

Secondly, consider the spatial evolution of the vortex. Setting $\alpha = \alpha_r + \boldsymbol{i}\alpha_i$ (complex), where α_r is the axial wavenumber, $-\alpha_i$ is the spatial growth rate and ω is the angular frequency (real) in (3.2); the spatial growth rate was obtained by solving (3.3). Figure 6(c,d) plots the growth rate $-\alpha_i$ and frequency ω as functions of the axial wavenumber α_r. Although the features are similar to those of the temporal

https://doi.org/10.1017/jfm.2020.388 Published online by Cambridge University Press

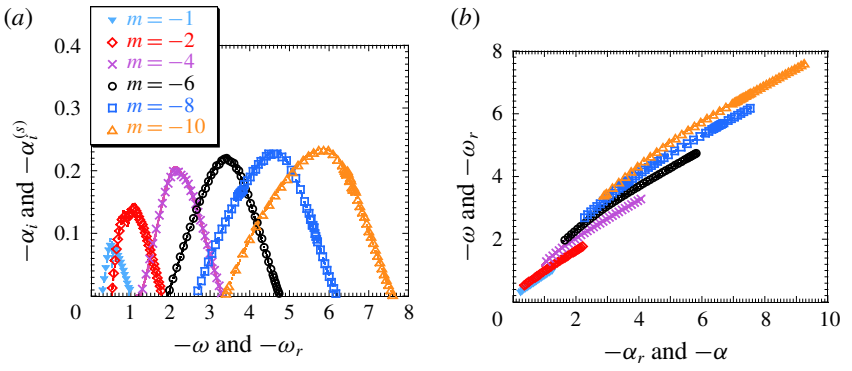


FIGURE 7. Comparisons of temporal growths and the spatial growth modes for various azimuthal wavenumbers, obtained by the Gaster transformation in (3.20): (*a*) growth rate versus frequency and (*b*) frequency versus axial wavenumber.

cases in figure 6(*a*,*b*), the profiles for $m = -1$ and -2 differ near the maximum growth rate. At the low wavenumbers, because the growth rates were small, crossing modes might occur in spatial growth.

Thirdly, to better understand the linear unstable property of vortices with helicity instability, we compared their temporal and spatial evolutions. If the local base flows are equal in both growth processes, the group velocity c_g of the spatial growth nearly matches that of the temporal growth. The following relation, called the Gaster transformation (Gaster 1968), then holds:

$$\omega^{(s)} = \omega_r, \quad \alpha_r^{(s)} = \alpha, \quad -\alpha_i^{(s)} = \frac{\omega_i}{c_g}, \quad c_g = \frac{\mathrm{d}\omega}{\mathrm{d}\alpha}. \tag{3.20a–d}$$

Here the spatial growth property (superscripted by s) is transformed from the temporal growth property. Figure 7 plots the growth rate versus frequency and the frequency versus axial wavenumber for various azimuthal wavenumbers. The symbols represent the eigenvalues of the spatial growth transformed from those of temporal growth by (3.20), and the curves are the spatial growth properties. The spatial growth ones were consistent with their transformed values except at some low wavenumbers. This result suggests that the initial spatial growth stage can be understood by obtaining the disturbance features of Batchelor vortices during temporal growth.

To investigate the disturbance structure associated with helicity instability at $q = 0.64$, $\mu = 0.8$ and $M_\infty = 2.5$, the eigenfunction profiles of the disturbance for $m = -4$ are plotted in figure 8. When $D = 0.125$ and 0.25, the base flows caused a competition among the velocity disturbances U, V and W at the outer edge of the vortex ($r \sim 1.8$). The radial velocity disturbance U was very much larger at $D = 0.125$ than in the conventional Batchelor vortex where the amplitude of the axial velocity disturbance is the largest (Delbende & Rossi 2005), strongly promoting spreading in the radial direction. When $D = 0.50$, although the velocity disturbances also existed at the outer edge of the vortex, the density disturbance was large and repressed the disturbance growth (Hiejima 2019). Accordingly, terms I and III exerted opposing effects on the growth property at $D = 0.50$. The phase profiles at $D \leqslant 0.25$ and $D = 0.50$ clearly differ in figure 8, and the phase change within $1.5 < r < 3.5$ depends on the helicity instability effect.

https://doi.org/10.1017/jfm.2020.388 Published online by Cambridge University Press

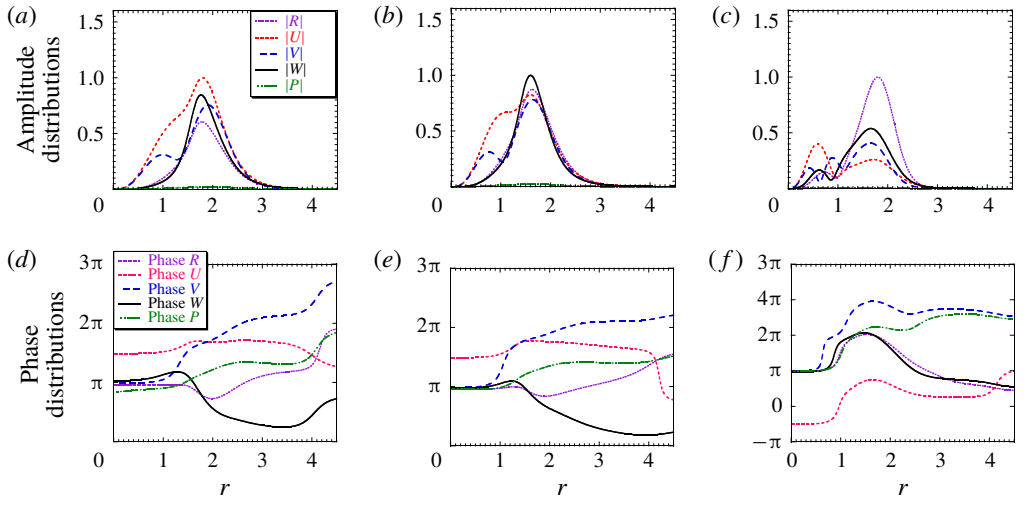


FIGURE 8. Eigenfunction profiles of the disturbance for $m=-4$, $q=0.64$ and $\mu=0.8$ at $M_\infty=2.5$. Shown are the amplitudes (*a–c*) and phases (*d–f*) at (*a*,*d*) $D=0.125$, (*b*,*e*) $D=0.25$ and (*c*,*f*) $D=0.50$.

4. Direct numerical simulations

4.1. *Governing equations*

From a natural transition perspective, the helicity effect on the spatial evolution of Batchelor vortices subjected to small random noise is investigated using three-dimensional numerical simulations. Note that the simulated velocities and pressure were normalised by using the free stream sonic velocity $c^*_\infty(=\sqrt{\gamma R^* T^*_\infty})$ rather than U^*_∞. The normalised governing equations were the three-dimensional, unsteady, compressible Navier–Stokes equations in general coordinates ξ_i ($i=1$–3), which are given as

$$\frac{\partial}{\partial t}\left(\frac{\boldsymbol{Q}}{J}\right)+\frac{\partial \boldsymbol{F}_i}{\partial \xi_i}=\frac{\partial \boldsymbol{F}_{vi}}{\partial \xi_i}, \tag{4.1}$$

$$\boldsymbol{Q}=\begin{bmatrix}\rho\\ \rho u_1\\ \rho u_2\\ \rho u_3\\ e\end{bmatrix},\quad \boldsymbol{F}_i=\begin{bmatrix}\rho U_i\\ \rho u_1 U_i+p(J^{-1}\partial\xi_i/\partial x_1)\\ \rho u_2 U_i+p(J^{-1}\partial\xi_i/\partial x_2)\\ \rho u_3 U_i+p(J^{-1}\partial\xi_i/\partial x_3)\\ (e+p)U_i\end{bmatrix},\quad \boldsymbol{F}_{vi}=\begin{bmatrix}0\\ \tau_{1k}(J^{-1}\partial\xi_i/\partial x_k)\\ \tau_{2k}(J^{-1}\partial\xi_i/\partial x_k)\\ \tau_{3k}(J^{-1}\partial\xi_i/\partial x_k)\\ \beta_k(J^{-1}\partial\xi_i/\partial x_k)\end{bmatrix},$$

$$J^{-1}=\frac{\partial x_1}{\partial \xi_1}\left(\frac{\partial x_2}{\partial \xi_2}\frac{\partial x_3}{\partial \xi_3}-\frac{\partial x_2}{\partial \xi_3}\frac{\partial x_3}{\partial \xi_2}\right)+\frac{\partial x_1}{\partial \xi_2}\left(\frac{\partial x_2}{\partial \xi_3}\frac{\partial x_3}{\partial \xi_1}-\frac{\partial x_2}{\partial \xi_1}\frac{\partial x_3}{\partial \xi_3}\right)+\frac{\partial x_1}{\partial \xi_3}\left(\frac{\partial x_2}{\partial \xi_1}\frac{\partial x_3}{\partial \xi_2}-\frac{\partial x_2}{\partial \xi_2}\frac{\partial x_3}{\partial \xi_1}\right),$$

$$U_i=\left(J^{-1}\frac{\partial \xi_i}{\partial x_k}\right)u_k,\quad \beta_i=u_k\tau_{ik}+q_i,$$

where $\boldsymbol{Q}$ is a vector of conservative variables, and $\boldsymbol{F}_i$ and $\boldsymbol{F}_{vi}$ contain the convective and viscous fluxes, respectively. The Jacobian J transforms the coordinate system from

https://doi.org/10.1017/jfm.2020.388 Published online by Cambridge University Press

the physical space to the computational space, $J^{-1}\partial\xi_i/\partial x_k$ are the derivatives of the coordinate conversion, i.e. the metrics, and U_i are the velocity components at the grid interface. The thermodynamics relation, the normalised equation of state and the transport coefficients are given as

$$e = \frac{p}{\gamma - 1} + \frac{1}{2}\rho u_k u_k, \quad p = \rho T,$$

$$\tau_{ij} = \frac{\eta(T)}{Re_M}\left(\frac{\partial u_i}{\partial x_j} + \frac{\partial u_j}{\partial x_i} - \frac{2}{3}\delta_{ij}\frac{\partial u_k}{\partial x_k}\right), \tag{4.2}$$

$$q_i = -\frac{\gamma}{(\gamma - 1)}\frac{\eta(T)}{Re_M Pr}\frac{\partial T}{\partial x_i}, \tag{4.3}$$

where e is the total energy, τ_{ij} is the viscous stress tensor, q_i is the conductive heat flux and u_i are the velocity components in Cartesian coordinates. The Reynolds number based on the sonic velocity is defined as $Re_M = (\rho^*_\infty c^*_\infty \delta^*_s)/\eta^*_\infty$ $(= Re/M_\infty)$, and the Prandtl number Pr is 0.72. The viscosity $\eta(T)$ is calculated from Sutherland's law, i.e.

$$\eta(T) = T^{3/2}\frac{1 + \vartheta}{T + \vartheta}, \tag{4.4}$$

where $\vartheta = 110.4/(\gamma T^*_\infty)$ is normalised by the free stream temperature.

4.2. *Numerical methods and computational conditions*

To investigate the helicity instability effects of Batchelor vortices, the small disturbances that evolve in supersonic flows must be simulated with sufficient accuracy. The convective flux was evaluated by a flux-splitting technique called the AUSMDV scheme (Wada & Liou 1994) and the weighted compact nonlinear scheme (Deng & Zhang 2000). The primitive variables at the grid interfaces were interpolated to ninth-order accuracy (Nonomura & Fujii 2013). Note that strong discontinuities such as shockwaves were absent in this system. The viscous flux terms were calculated to eighth-order accuracy by a central difference method. The temporal integration adopted a four-step, fourth-order accuracy scheme (Jameson, Schmidt & Turkel 1981).

The purpose of the simulations was to prove that the stability of Batchelor vortices with large q is linked to helicity effects, as demonstrated in the stability analysis in § 3. The physical domain was a rectangular box with sides $L_x = 300$, $L_y = 40$ and $L_z = 40$ at resolutions of $N_x = 901$, $N_y = 281$ and $N_z = 281$, respectively. The grid spacing was uniform in the x direction. To capture the helicity effect by which the evolution spreads in the radial direction, the grid spacing in the y and z directions was uniform over a space that extended symmetrically from the vortex axis to six times the radius of the vortex core. Beyond this region, the grid splayed out at irregular intervals. Note that the vortex core radius was close to the radial distance of the maximum azimuthal velocity. The inflows, introduced from the left boundary in the x direction, were fixed Batchelor vortices with added random disturbances (white noise). The amplitude of the random noise was 3 % of the mainstream flow amplitude. The nonlinear evolutions of the Batchelor vortex with large q were numerically simulated from a natural transition perspective under two conditions: $M_\infty = 2.5$ ($q = 0.64$, $\mu = 0.8$) and $M_\infty = 5.0$ ($q = 0.36$, $\mu = 0.8$). The Reynolds number Re_M was fixed at 9000, and the helicity parameter D was varied as 0.125, 0.25, 0.50 and 1.0. The outflow

https://doi.org/10.1017/jfm.2020.388 Published online by Cambridge University Press

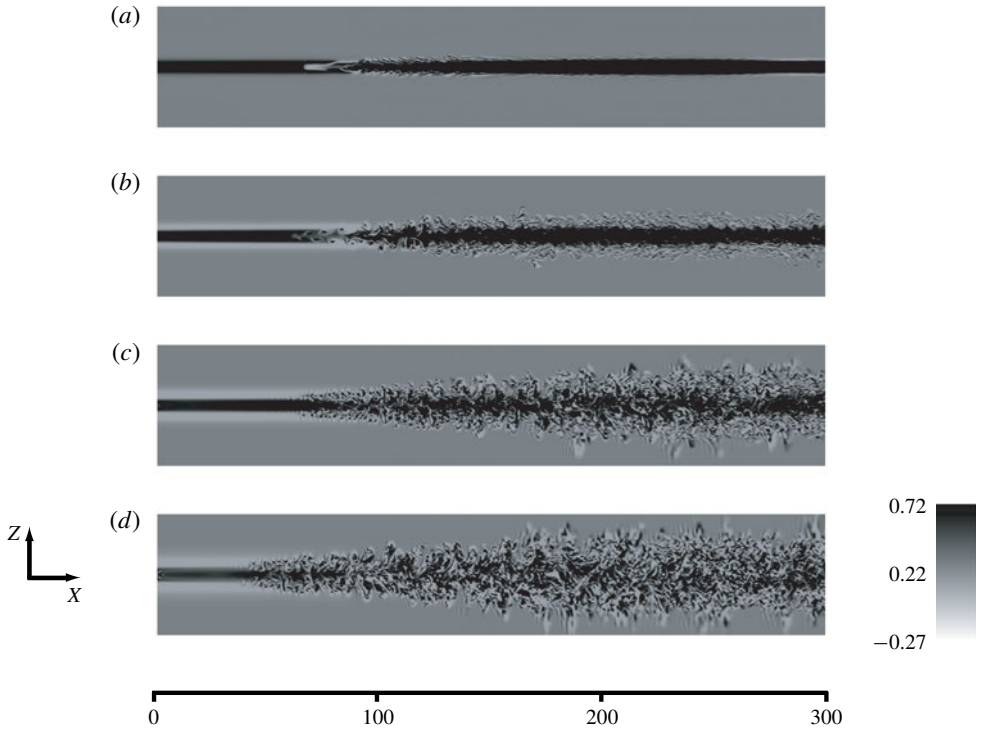


FIGURE 9. Evolutions of Batchelor vortices ($M_\infty = 2.5$, $q = 0.64$, $\mu = 0.8$) under random disturbance, showing the cross-sections of the helicity density contours along the vortex axis: (*a*) $D = 1.0$, (*b*) $D = 0.5$, (*c*) $D = 0.25$ and (*d*) $D = 0.125$. Positive and negative helicities are rendered in black and white, respectively.

condition at $x = L_x$ was extrapolated to the zeroth order. To simulate an isolated vortex without a contaminated centre, symmetry conditions were imposed on the boundary surfaces composing the x–y and x–z planes because the mirror effect of the symmetry boundary condition was diminished at $L_y = L_z = 40$. This numerical approach was validated in the appendix of reference (Hiejima 2019).

5. Nonlinear developments of Batchelor vortices

5.1. *Effect of helicity instability*

This subsection describes the nonlinear evolutions of Batchelor vortices associated with helicity instability. Helicity contours provide useful information about the transition processes of vortices. The spatial developments of a Batchelor vortex with large q are revealed in figures 9 and 10, which show the helicity density contours in the x–z cross-sections along the vortex axis at $M_\infty = 2.5$ ($q = 0.64$, $\mu = 0.8$) and $M_\infty = 5.0$ ($q = 0.36$, $\mu = 0.8$), respectively. Evidently, helicity has a great effect on vortex structure (Moffatt & Tsinober 1992).

In the $M_\infty = 2.5$ case with $D = 1.0$, weak instability developed inside the vortex core and along the outer edge of the vortex, but the system was stabilised downstream. Note that a conventional Batchelor vortex with $D = 1.0$ is exposed to disturbances that grow near the vortex centre (Delbende & Rossi 2005). When D reduced to 0.50, spiral fluctuations developed inside the vortex core, followed by a fluctuation

https://doi.org/10.1017/jfm.2020.388 Published online by Cambridge University Press

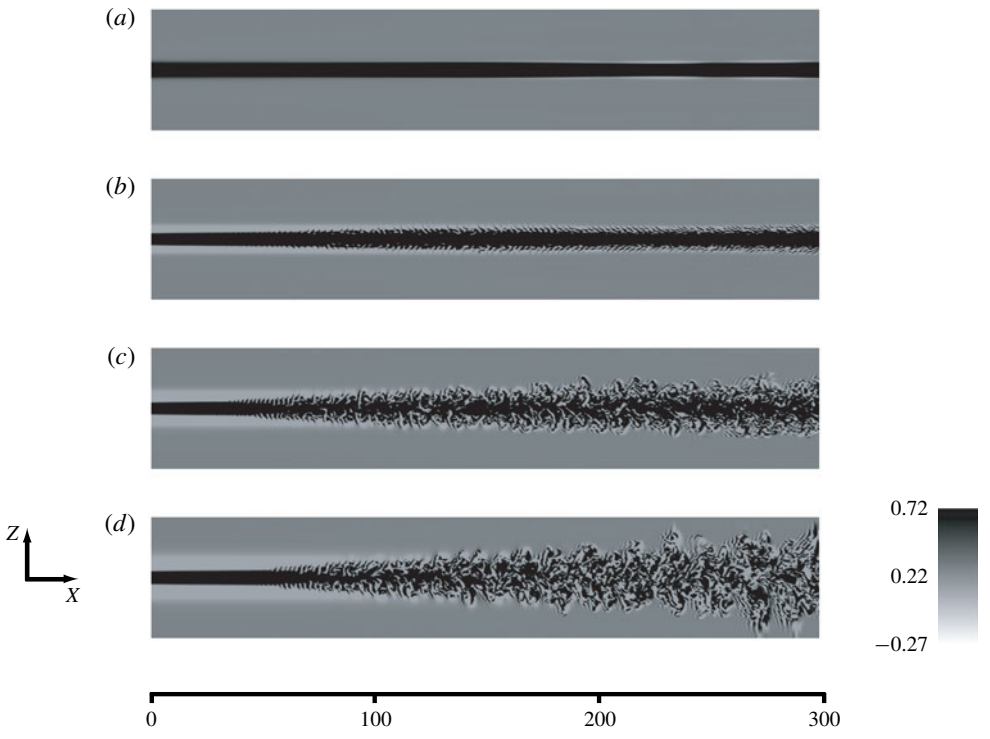


FIGURE 10. Evolutions of Batchelor vortices ($M_\infty = 5.0$, $q = 0.36$, $\mu = 0.8$) under random disturbance, showing the cross-sections of the helicity density contours along the vortex axis: (*a*) $D = 1.0$, (*b*) $D = 0.5$, (*c*) $D = 0.25$ and (*d*) $D = 0.125$. Positive and negative helicities are rendered in black and white, respectively.

growth near the negative helicity region (see figure 3). Observing the pronounced internal growth in conventional Batchelor vortices and the external growth induced by helicity effects in the evolution is a valuable outcome of this approach. At $D = 0.25$, fluctuations developed at the interface between the positive and negative helicity profiles. In the initial development stage, these fluctuations consisted of high wavenumber modes (higher than those obtained from $q = 0.16$ (Hiejima 2015*a*)). In addition, many small-scale developments (such as incompressible evolutions) occurred downstream. At $D = 0.125$, the structure was dominated by small scales on the outer edge of the vortex, and the considerable radial spreading of the fluctuation suggested a growth beyond evolutions due to entropy instability (Hiejima 2019). This demonstrates a tremendous development as a natural transition in supersonic flows. Thus, the observed vortex evolutions for different values of the parameter D were consistent with the helicity instability features determined in the stability analysis (§ 3.2).

Let us discuss the case of $M_\infty = 5.0$. In contrast to the case of $M_\infty = 2.5$, no disturbance growth was seeded from the vortex core, and each vortex was disrupted by helicity instability. At $D = 1.0$, the vortex flow was stable with some fluctuations (white regions) at the outer vortex. However, this feature differed from that of asymptotic analysis at high wavenumbers in figure 2(*d*). At $D = 0.50$, clear disturbance growths were induced by the helicity profile. In the early development stage, spiral

https://doi.org/10.1017/jfm.2020.388 Published online by Cambridge University Press

structures appeared as a wrinkled rim in the cross-sections (see also figure 12). Although the evolution was dominated by helicity instability, the radial spreading fluctuation was weak. At $D = 0.25$, the small fluctuations generated from the outer edge of the vortex did not extend to the neighbourhood of the vortex axis, and the spreading rate was weaker than at $D = 0.25$ in the $M_\infty = 2.5$ case. This case showed the earliest transition, consistent with the result in figure 3. When D was further reduced to 0.125, small downstream scales appeared despite the high $M_\infty = 5.0$. Jacquin & Pantano (2002) showed that turbulence produced within the Batchelor vortex core must overcome the dispersion buffer adjacent to the vortex core before the turbulent fluctuations can reach the vortex periphery. The D-dependent helicity instability originally grew at the outer edge of the vortex, suggesting that helicity instability might overcome the rotational stabilization in conventional Batchelor vortices with large q.

5.2. *Evolution of circulation profiles and vortical structures*

This subsection investigates the difference between helicity instability and the centrifugal instability associated with conventional Batchelor vortices. A centrifugal instability derived by Rayleigh (1917) develops on the circulation profiles of rotational flows (Drazin & Reid 1981). This instability arises when the mean circulation reduces in the radial direction (Uberoi 1979) owing to circulation overshoot (Govindaraju & Saffman 1971) in a turbulent line vortex. Figure 11 shows the mean circulation profiles $\overline{\Gamma}/M_\infty$ for various D at $M_\infty = 2.5$ and 5.0. The circulation profiles were more affected by D than by the Mach number effect. At $D = 1.0$, the vortices were stable throughout the spatial evolution. When D reduced to 0.50, weak circulation overshoots indicating centrifugal instability appeared near the vortex core. At $D = 0.25$ and 0.125, the circulation overshoot appeared at the outer side of the vortex core, where fluctuations resulted from the helicity profiles. Note that these fluctuations ranged over the regions of phase change ($0 < r < 4$) in figure 8. In conventional Batchelor vortices, the circulation overshoot decreases with increasing q because the outward spread of fluctuations is suppressed, thereby enhancing the rotational stabilisation (Jacquin & Pantano 2002; Delbende & Rossi 2005). However, despite the large q, moderate circulation overshoots that characterise small q (Hiejima 2015*a*) appear at a point distant from the core. These profiles also differ from the circulation profile of the isentropic vortex at $q = 0.16$, which strengthens the centrifugal instability (Hiejima 2014). It follows that the features of helicity instability differ from those of centrifugal instability.

As described in § 5.1, the spatial evolutions of the vortices at $M_\infty = 5.0$ and large D apparently differed from those of the linear stability analysis. Figure 12 shows the isosurfaces of the second invariant of the velocity gradient tensor $\mathcal{Q}$ ($= -0.01$), which are useful for quantitatively visualising the vortical structures, at $M_\infty = 5.0$, $q = 0.36$, $\mu = 0.8$, and four values of D. The $\mathcal{Q}$ is calculated by

$$\mathcal{Q} = \tfrac{1}{2}(-S_{ij}S_{ij} + R_{ij}R_{ij} + \mathcal{P}^2), \tag{5.1}$$

$$S_{ij} = \frac{1}{2}\left(\frac{\partial u_j}{\partial x_i} + \frac{\partial u_i}{\partial x_j}\right), \quad R_{ij} = \frac{1}{2}\left(\frac{\partial u_j}{\partial x_i} - \frac{\partial u_i}{\partial x_j}\right), \quad \mathcal{P} = \frac{\partial u_k}{\partial x_k},$$

where S_{ij} and R_{ij} are the strain rates and vorticity tensors, respectively, which respectively contain the symmetric and asymmetric components of the velocity gradient tensor $\partial u_i/\partial x_j$ and $\mathcal{P}$ is the divergence of the velocity vectors (Jeong &

https://doi.org/10.1017/jfm.2020.388 Published online by Cambridge University Press

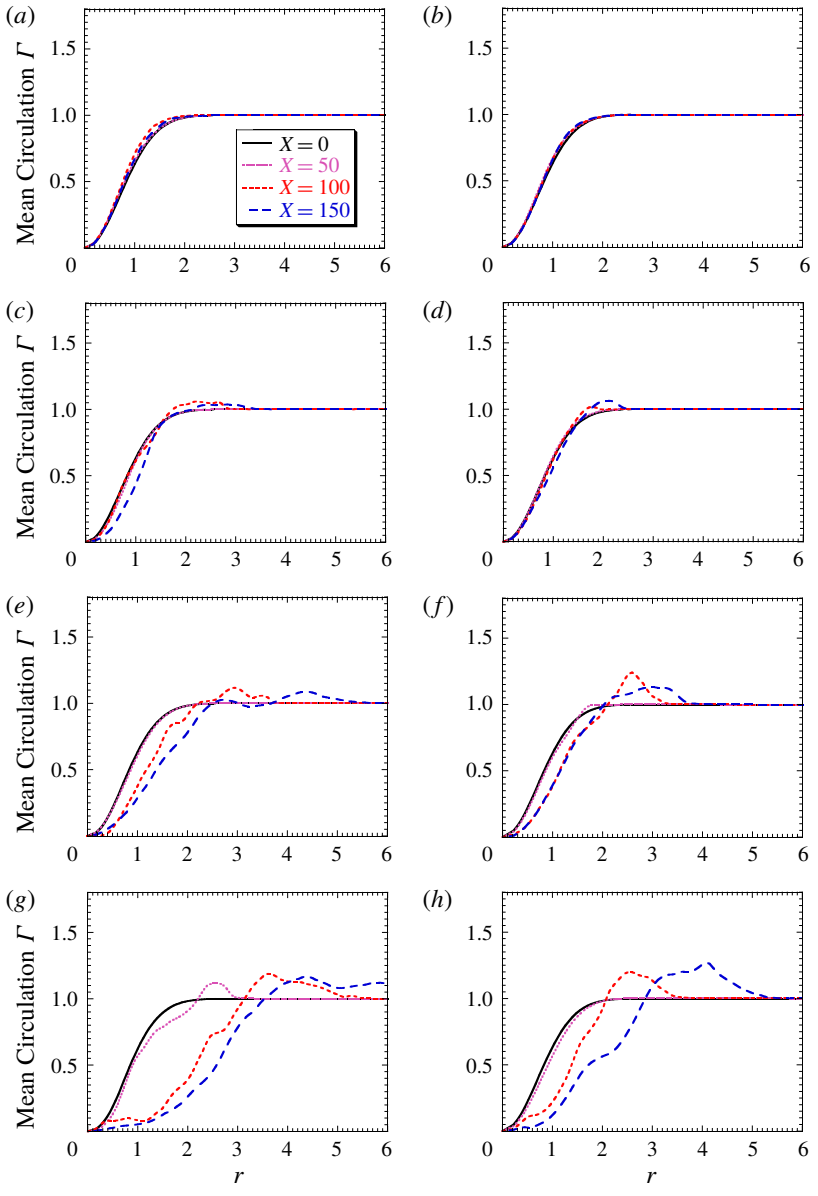


FIGURE 11. Mean circulation profiles $\overline{\Gamma}/M_\infty$: (*a*,*c*,*e*,*g*) $M_\infty = 2.5$, $q = 0.64$, $\mu = 0.8$ and (*b*,*d*,*f*,*h*) $M_\infty = 5.0$, $q = 0.36$, $\mu = 0.8$, and (*a*,*b*) $D = 1.0$, (*c*,*d*) $D = 0.50$, (*e*,*f*) $D = 0.25$, (*g*,*h*) $D = 0.125$.

Hussain 1995). As seen in figure 12, the parameter D clearly affected the evolution. At $D = 1.0$, the vortex was completely stable, but at $D = 0.50$, weak spiral structures appeared after the transition with little outward extension in the radial direction. When D was reduced to 0.25 and 0.125, the vortical structures largely differed from those at $D = 0.50$ because strong fluctuation growths were induced by the helicity instability. In the early stage of the evolutions, random disturbances generated spiral structures with a high wavenumber due to the large q. At $D = 0.125$, the outward

https://doi.org/10.1017/jfm.2020.388 Published online by Cambridge University Press

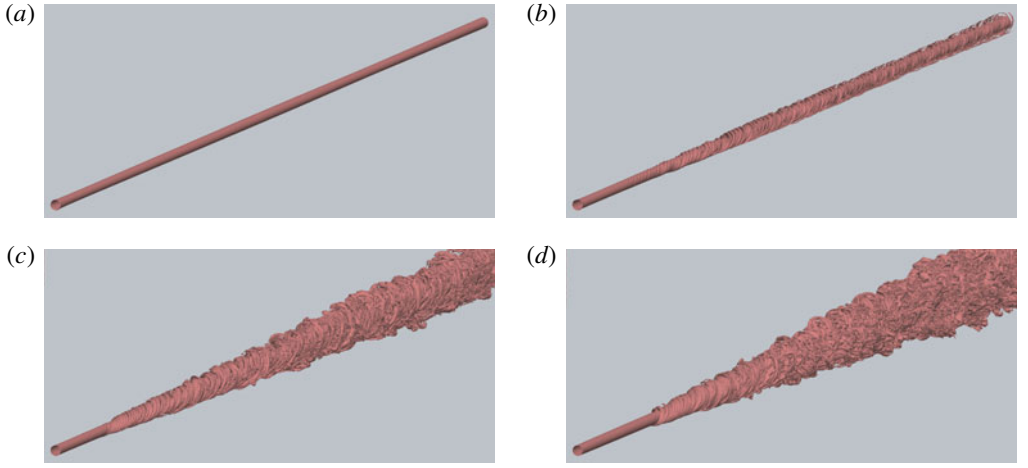


FIGURE 12. Isosurfaces of the second invariant of the velocity gradient tensor $\mathcal{Q}$ at $M_\infty = 5.0$, $q = 0.36$ and $\mu = 0.8$: (*a*) $D = 1.0$, (*b*) $D = 0.50$, (*c*) $D = 0.25$ and (*d*) $D = 0.125$.

spreading was considerably enlarged and the downstream scales were much smaller than in the case of $D = 0.25$ (see also figure 10*c*,*d*). The eddy generation (in terms of number of eddies) was vastly superior to that of isentropic-vortex effects under uniform stagnation-temperature conditions at $M_\infty = 5.0$ (Hiejima 2019). Therefore, these evolution results at small D demonstrate the great effect of helicity instability (term III in (3.6)).

5.3. *Unstable modes selected by random disturbance*

From a transition perspective, it is important to understand how modes evolve from random disturbances. This subsection focuses on the growth modes during the vortex development and, hence, elucidates the specific property of Batchelor vortices associated with helicity instability. As shown in figure 6, the axial wavenumber α_r increases with azimuthal wavenumber m, implying that the discrimination of the modes in swirling flows is m rather than α_r. Thus, the mode decomposition of m was investigated in the spatially developing flows. The flow fluctuations were decomposed by taking the Fourier transform of m,

$$\mathscr{F}_m(\Phi, x, r, t) = \frac{1}{2\pi}\int_0^{2\pi} \Phi(x, r, t, \theta)\mathrm{e}^{im\theta}\,\mathrm{d}\theta, \tag{5.2}$$

where $\Phi(x, r, \theta)$ represents a physical variable. For the axial vorticity $\Phi(x, r, \theta) = \omega_x$, the amplitude of the axial vorticity fluctuation Ω_x is determined as

$$|\Omega_x| = |\mathscr{F}_m(\omega_x, x, r, t)|. \tag{5.3}$$

Figures 13 and 14 show the amplitude profiles of the axial vorticity fluctuations calculated by (5.3) for eight azimuthal wavenumbers at $M_\infty = 2.5$ ($q = 0.64$, $\mu = 0.8$) and $M_\infty = 5.0$ ($q = 0.36$, $\mu = 0.8$). In the $M_\infty = 2.5$ case with $D = 0.125$ at $x = 30$, some high azimuthal wavenumbers competed around $r = 2$. When $D = 0.25$ at $x = 50$, the peak value of the most unstable mode ($m = -6$) coincided with the extremum of

https://doi.org/10.1017/jfm.2020.388 Published online by Cambridge University Press

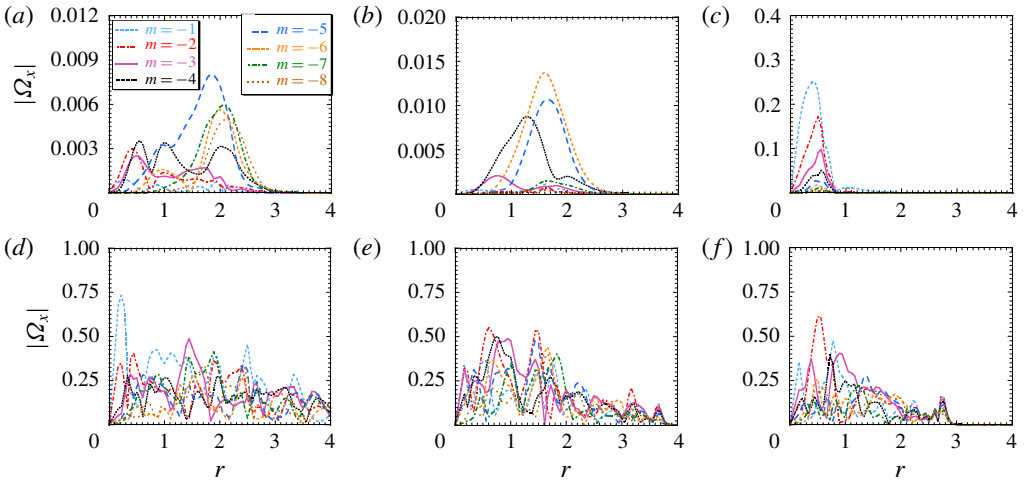


FIGURE 13. Amplitude profiles of the axial vorticity fluctuations obtained in the mode analysis for various azimuthal wavenumbers at $M_\infty = 2.5$, $q = 0.64$ and $\mu = 0.8$: (*a*) $D = 0.125$, $x = 30$; (*b*) $D = 0.25$, $x = 50$; (*c*) $D = 0.50$, $x = 65$; (*d*) $D = 0.125$, $x = 100$; (*e*) $D = 0.25$, $x = 100$; and (*f*) $D = 0.50$, $x = 100$.

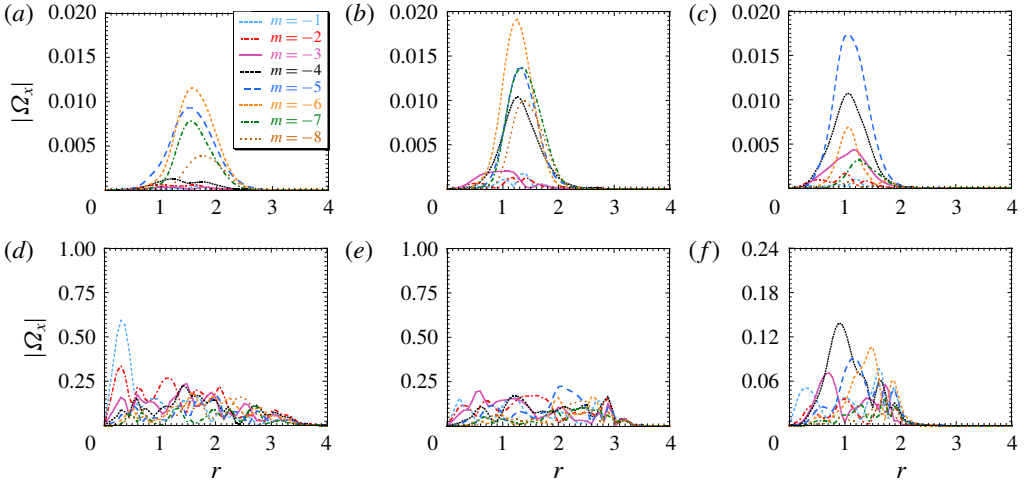


FIGURE 14. Amplitude profiles of the axial vorticity fluctuations obtained in the mode analysis for various azimuthal wavenumbers at $M_\infty = 5.0$, $q = 0.36$ and $\mu = 0.8$: (*a*) $D = 0.125$, $x = 50$; (*b*) $D = 0.25$, $x = 35$; (*c*) $D = 0.50$, $x = 50$; (*d*) $D = 0.125$, $x = 100$; (*e*) $D = 0.25$, $x = 100$; and (*f*) $D = 0.50$, $x = 100$.

the negative helicity profile in figure 3. These two cases robustly express the feature of helicity instability. In contrast, when $D = 0.50$ at $x = 65$, the fluctuation growth appeared inside the vortex core ($r < 1$; see figure 9*b*). In addition, the linear unstable mode (exponential growth) was suppressed because low azimuthal wavenumbers dominated in this case; growth of the $m = -1$ mode, which is strongly related to vortex breakdown (Qadri, Mistry & Juniper 2013), was observed. Abid (2008) suggested that transient growth can trigger nonlinearities near the vortex axis.

https://doi.org/10.1017/jfm.2020.388 Published online by Cambridge University Press

Thus, this development is not caused by the helicity instability found in § 3. In the cases of $D = 0.125$ and 0.25 at $x = 100$, fluctuations spread to approximately four times the vortex core. In Batchelor vortices, a large fluctuation on the outer edge of the vortex is necessary to restrain a stabilising mechanism with large q (Jacquin & Pantano 2002). Helicity instability satisfies this necessary condition. Note that the fluctuation amplitude at $x = 100$ in these figures is attributed to the changing mean flow in the downstream (see figure 11). Regardless of D, the amplitude profiles at $M_\infty = 5.0$ display the helicity instability feature, namely, several high-azimuthal-wavenumbers grow at the highly sensitive point (negative helicity region) at which the helicity profiles develop instabilities, as shown in the top panels of figure 14. Moreover, the outward spreading was weak at $D = 0.50$ (figure 14*f*). These results accorded with the helicity contours in figure 10. However, for all values of D, the magnitudes of these fluctuations were smaller than for $M_\infty = 2.5$ at $x = 100$. Even though helicity instability is observed, the results suggest that there are compressibility effects due to the Mach number in spatial evolutions.

As discussed above, the mode decompositions (except those of figure 13*c*,*f*) were characterised by high azimuthal wavenumbers caused by the large q and the helicity profiles. Although vortex breakdown is characterised by a low-wavenumber mode, no supersonic vortex breakdown (i.e. disappearances of the vortex axes (Hiejima 2017)) appeared in figures 9 and 10. Note that the two cases considered here do not satisfy the onset condition (Hiejima 2018) because of $q/\mu = 0.8$ at $M_\infty = 2.5$ and $q/\mu = 0.45$ at $M_\infty = 5.0$. Therefore, the present results also support the previous results of vortex breakdown in supersonic flows.

Figures 13 and 14 reveal a predominance of high azimuthal wavenumbers near the minimum of the helicity profiles during the early evolution stage under random noise. Mode selection mechanisms are connected to the local stability properties of flows (Viola *et al.* 2016). Understanding how the growth property is governed by natural selection is essential for elucidating the instability phenomena. The maximum growth rate is related to the fluctuations in kinetic energy $\hat{K}$, obtained by integrating the square of the velocity fluctuation $\hat{u}_k$,

$$\hat{K} = \int_A \frac{1}{2}\overline{\rho}\,\hat{u}_k\hat{u}_k \,\mathrm{d}A, \tag{5.4}$$

where the '—' and '$\wedge$' symbols denote the mean and fluctuating components, respectively, and A is the cross-sectional area in a plane perpendicular to the axial flow at some x. The velocity fluctuation $\hat{u}_k$ is approximated by

$$\hat{u}_k \sim C\mathrm{e}^{-\alpha_i x}. \tag{5.5}$$

Note that C depends on y and z in the cross-sectional area. Substituting (5.5) into (5.4), $\hat{K}$ is given by

$$\hat{K} \sim \mathrm{e}^{-2\alpha_i x}F(A), \tag{5.6}$$

where $F(A)$ is found by integrating (5.4) at the given x. Taking the logarithm of both sides of (5.6) gives

$$\tfrac{1}{2}\log_e \hat{K} \sim -\alpha_i x + \tfrac{1}{2}\log_e[F(A)]. \tag{5.7}$$

Differentiating (5.7) and neglecting the last term, we finally obtain

$$\frac{1}{2}\frac{\mathrm{d}}{\mathrm{d}x}(\log_e \hat{K}) \sim -\alpha_i. \tag{5.8}$$

https://doi.org/10.1017/jfm.2020.388 Published online by Cambridge University Press

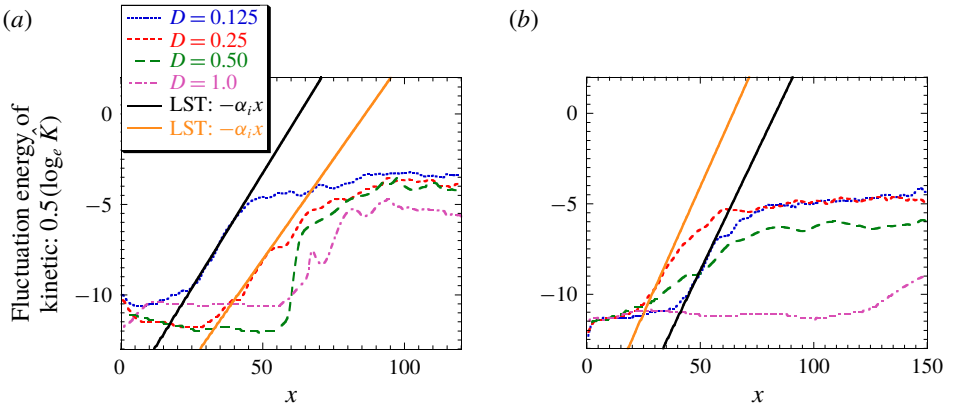


FIGURE 15. Streamwise variations in kinetic energy fluctuations ($0.5 \log_e \hat{K}$) obtained from direct numerical simulations at various D and (*a*) $M_\infty = 2.5$, $q = 0.64$, $\mu = 0.8$ and (*b*) $M_\infty = 5.0$, $q = 0.36$, $\mu = 0.8$. The black ($D = 0.125$) and yellow ($D = 0.25$) straight lines represent the spatial growth rates $-\alpha_i$ listed in table 1.

M_∞	q	μ	D	m	$-\alpha_i$
2.5	0.64	0.8	0.125	−5	0.25044
2.5	0.64	0.8	0.25	−6	0.22286
5.0	0.36	0.8	0.125	−6	0.26221
5.0	0.36	0.8	0.25	−6	0.28083

TABLE 1. Maximum spatial growth rates $-\alpha_i$ obtained from linear stability analysis in § 3.3.

Figure 15 plots the simulated streamwise variations in the kinetic energy fluctuations ($0.5 \log_e \hat{K}$) at various D in the $M_\infty = 2.5$ and $M_\infty = 5.0$ cases. For comparison, the spatial growth rates $-\alpha_i$ listed in table 1, which are obtained from linear stability analysis in § 3.3, are also plotted as straight lines. Note that the fluctuation magnitude is plotted on the logarithmic scale. In the $M_\infty = 2.5$ case, the initial energy evolution at $D = 0.125$ and 0.25 was dominated by linear unstable modes. However, at $D = 0.50$ and 1.0, the energy fluctuations demonstrated the features of nonlinear growth through different transitions. Abid (2008) attributed the discrepancy between the nonlinear evolution and the linear unstable modes to transient growth. As nonlinear effects were negligible at low initial energy, transient growth can be expected in the large energy case ($q = 0.64$). In the $M_\infty = 5.0$ case with $D = 0.125$ and 0.25, the linear growth regions were short-lived and the spatial growth rates in the linear stability analysis coincided with the simulation results. At $D = 0.50$, the linear growth rate was comparable to that at $D = 0.125$ and 0.25 (figure 2*b*), but the most unstable mode in the linear stability analysis was not contributed to by random noise in the flow (see figure 14*c*,*f*). In this case, the helicity instability occurred at the outer side of the vortex core, but was subdued. At $D = 1.0$, the growth was slow and weak. Consequently, under the $D \leqslant 0.25$ conditions with a relatively large growth rate, the evolution raised the linear disturbances.

https://doi.org/10.1017/jfm.2020.388 Published online by Cambridge University Press

6. Concluding remarks

The stabilisation mechanism of inviscid modes in compressible Batchelor vortices with a large swirl number has been studied from a different angle. In general swirling wakes, the growth rate equation was divisible into four terms describing different instability properties in asymptotic analysis of linear stability theory (Hiejima 2015*b*). Although helicity instability that manifests as negative helicity profiles was found, the instability at large swirl numbers has not been clarified. This paper investigated the feature of helicity instability and the transition process to large-q compressible Batchelor vortices in detail. The investigation was performed by linear stability analysis and direct numerical simulations.

The present study confirmed that the helicity instability destabilises Batchelor vortices with a large swirl number q, which has not been previously reported. In the asymptotic analysis, increasing the azimuthal vorticity thickness (i.e. decreasing D) enhanced the helicity instability at the outer edge of the vortex. The same feature was observed in the temporal and spatial growth rates of linear stability analysis. At large q and $D = 1.0$, the helicity profile exerted a stabilising effect. This finding explains why conventional Batchelor vortices with large swirl numbers remain stable. To clarify their response to small random disturbances in linear and nonlinear states, spatially developing Batchelor vortices were numerically simulated at Mach numbers 2.5 and 5.0. The nonlinear simulations reconfirmed the effect of helicity instability. At small D, the nonlinear developments yielded a large fluctuation field with many small scales and high radial spreading rates in the supersonic flows. The instability was characterised by large fluctuations growing in the negative helicity region. This result crucially explains the retained fluctuation and can potentially destroy the compressibility effects. At high Mach numbers, the destabilisation effect of negative helicity is far superior to that of entropy gradient (Hiejima 2019) under uniform stagnation-temperature conditions.

For incompressible cases, the study of Viola *et al.* (2016), where forcing frequencies were used, is of great value in understanding of transition. However, the transition of compressible Batchelor vortices remains to be elucidated. How the unstable mode is selected and developed under small random noise is important for understanding natural transitions in vortex evolutions. When D was small, the transition process was dominated by linear unstable modes (exponential growth). In contrast, when D was large (even though the linear growth rates were large at $M_\infty = 5.0$), transient growths occurred as the nonlinearity effects were raised. This result might reflect the sensitivity of incompressible Batchelor vortices to transient growth under inviscid conditions (Heaton & Peake 2006). The nature and amplitude of the noise needs further consideration in this research framework.

Acknowledgements

This work was partly achieved through the use of large-scale computer systems SX–ACE at the Cybermedia Centre, Osaka University and was supported by JSPS KAKENHI, grant no. JP17K05145. The author expresses his deep gratitude to the anonymous referees for helping to improve the paper.

Declaration of interests

The author reports no conflicts of interest.

https://doi.org/10.1017/jfm.2020.388 Published online by Cambridge University Press

Appendix A. The case of axial flow with jet

The Batchelor vortex is originally a wake type for the axial velocity profile ($0 < \mu \leqslant U_\infty$). In terms of the generality of stabilities, this appendix deals with the case of axial flow with jet because temporal stability should not be affected by a Galilean change of reference frame in the incompressible framework. Let us consider U_∞ added an axial constant velocity to the base flow in (2.8):

$$u_x(r) = U_\infty - \mu \mathrm{e}^{-Dr^2}. \tag{A 1}$$

Figure 16 shows the helicity density and the distributions of the squared growth rate χ_0^2 of terms I–III in (3.6) for $U_\infty = -1.0$ and 1.0 in (A 1). The helicity profiles are significantly changed by the addition of an axial constant velocity to the base flow. However, as seen from the black lines in figure 16(*b*,*e*,*c*,*f*), the addition does not affect the stability; particularly, when $D < 1.0$, the instability is dominant in the outer side of the vortex core and when $D > 1.0$, the instability occurs in the core. For the jet type at $U_\infty = -1.0$, the sign of helicity is not related to the result of each term and the effect of separating terms II and III is not large because a sufficient condition for instability of swirling jets is satisfied if term II plus term III is positive (Hiejima 2015*b*). In contrast, for the wake type at $U_\infty = 1.0$, the negative helicity profile is surely connected to the instability due to term III at $D < 1.0$ and the growth rate is associated with the instability due to term II at $D > 1.0$. Therefore, the separation between terms II and III in the present Batchelor vortex (2.8) is valuable for the classification of instability under a wake condition without reverse flow: $0 < \mu \leqslant U_\infty$.

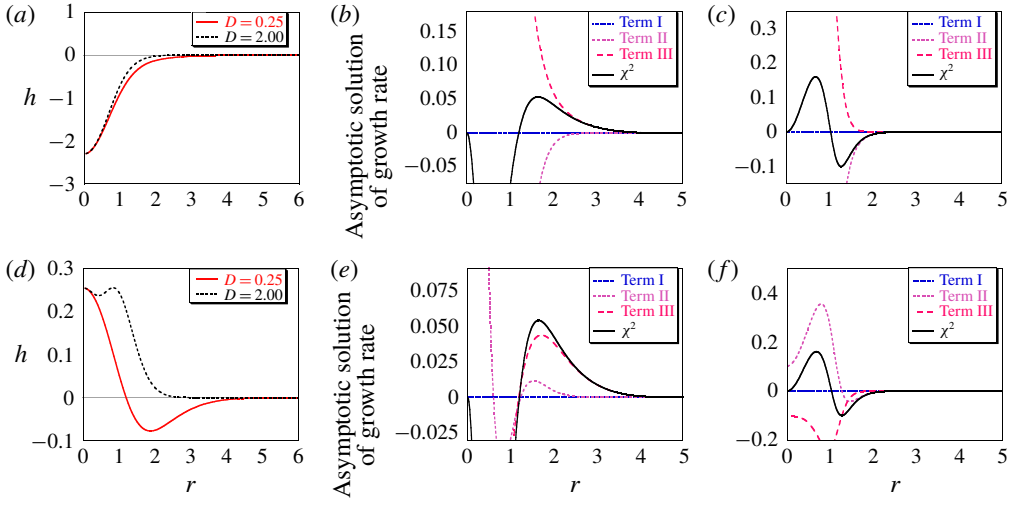


FIGURE 16. (Top row) Jet-type flow at $U_\infty = -1.0$ and (bottom row) wake-type flow at $U_\infty = 1.0$: (*a*,*d*) helicity density profiles; (*b*,*e*) $D = 0.25$ and (*c*,*f*) $D = 2.0$ profiles of squared temporal growth rates χ_0^2 for each term in (3.6), obtained for a Batchelor vortex with $q = 0.64$ and $\mu = 0.8$ at $M_\infty = 0.01$.

REFERENCES

ABID, M. 2008 Nonlinear mode selection in a model of trailing line vortices. *J. Fluid Mech.* **605**, 19–45.

https://doi.org/10.1017/jfm.2020.388 Published online by Cambridge University Press

ALEKSEENKO, S. V., KUIBIN, P. A. & OKULOV, V. L. 2007 *Theory of Concentrated Vortices. An Introduction*. Springer.

BATCHELOR, G. K. 1964 Axial flow in trailing line vortices. *J. Fluid Mech.* **20**, 645–658.

BILLANT, P. & GALLAIRE, F. 2013 A unified criterion for the centrifugal instabilities of vortices and swirling jets. *J. Fluid Mech.* **734**, 5–35.

BOGDANOFF, D. 1983 Compressibility effects in turbulent shear layers. *AIAA J.* **21**, 926–927.

BROADHURST, M. S. & SHERWIN, S. J. 2008 Helical instability and breakdown of a Batchelor trailing vortex. In *Prog. in Industrial Mathematics at ECMI 2006. Mathematics in Industry*, pp. 191–195. Springer.

CATTAFESTA, L. N. & SETTLES, G. S. 1992 Experiments on shock/vortex interaction. *AIAA Paper* 92–0315.

CLEMENS, N. T. & MUNGAL, M. G. 1995 Large-scale structure and entrainment in the supersonic mixing layer. *J. Fluid Mech.* **284**, 171–216.

DELBENDE, I., CHOMAZ, J.-M. & HUERRE, P. 1998 Absolute/convective instabilities in the Batchelor vortex: a numerical study of the linear impulse response. *J. Fluid Mech.* **355**, 229–254.

DELBENDE, I. & ROSSI, M. 2005 Nonlinear evolution of a swirling jet instability. *Phys. Fluids* **17**, 044103.

DENG, X. & ZHANG, H. 2000 Developing high-order weighted compact nonlinear schemes. *J. Comput. Phys.* **165**, 22–44.

DI PIERRO, B. & ABID, M. 2010 Instabilities of variable-density swirling flows. *Phys. Rev.* E **82**, 046312.

DI PIERRO, B. & ABID, M. 2011 Energy spectra in a helical vortex breakdown. *Phys. Fluids* **23**, 025104.

DI PIERRO, B. & ABID, M. 2012 Rayleigh–Taylor instability in variable density swirling flows. *Eur. Phys. J.* B **85**, 69.

DIMOTAKIS, P. E. 1991 Turbulent free shear layer mixing and combustion. In *High Speed Flight Propulsion Systems* (ed. S. Murthy & E. Curran), vol. 137, chap. 5, pp. 265–340. Progress in Astronautics and Aeronautics, AIAA.

DRAZIN, P. G. & REID, W. H. 1981 *Hydrodynamic Stability*. Cambridge University Press.

DUCK, P. W. & FOSTER, M. R. 1980 The inviscid stability of a trailing line vortex. *Z. Angew. Math. Phys.* **31** (4), 524–532.

DURAISAMY, K. & LELE, S. K. 2008 Evolution of isolated turbulent trailing vortices. *Phys. Fluids* **20** (3), 035102.

ECKHOFF, K. S. & STORESLETTEN, L. 1978 A note on the stability of steady inviscid helical gas flow. *J. Fluid Mech.* **89**, 401–411.

FABRE, D. & JACQUIN, L. 2004 Viscous instabilities in trailing vortices at large swirl numbers. *J. Fluid Mech.* **500**, 239–262.

GASTER, M. 1968 Growth of disturbances in both space and time. *Phys. Fluids* **11** (4), 723–727.

GOVINDARAJU, S. P. & SAFFMAN, P. G. 1971 Flow in a turbulent trailing vortex. *Phys. Fluids* **14** (10), 2074–2080.

GREEN, S. I. 1995 *Fluid Vortices*. Kluwer.

HEATON, C. J. 2007 Centre modes in inviscid swirling flows and their application to the stability of the Batchelor vortex. *J. Fluid Mech.* **576**, 325–348.

HEATON, C. J., NICHOLS, J. W. & SCHMID, P. J. 2009 Global linear stability of the non-parallel Batchelor vortex. *J. Fluid Mech.* **629**, 139–160.

HEATON, C. J. & PEAKE, N. 2006 Algebraic and exponential instability of inviscid swirling flow. *J. Fluid Mech.* **565**, 279–318.

HEATON, C. J. & PEAKE, N. 2007 Transient growth in vortices with axial flow. *J. Fluid Mech.* **587**, 271–301.

HIEJIMA, T. 2013 Linear stability analysis on supersonic streamwise vortices. *Phys. Fluids* **25**, 114103.

HIEJIMA, T. 2014 Spatial evolution of supersonic streamwise vortices. *Phys. Fluids* **26**, 074102.

HIEJIMA, T. 2015*a* A factor involved in efficient breakdown of supersonic streamwise vortices. *Phys. Fluids* **27**, 034103.

HIEJIMA, T. 2015*b* Stability of compressible streamwise vortices. *Phys. Fluids* **27**, 074107.

https://doi.org/10.1017/jfm.2020.388 Published online by Cambridge University Press

HIEJIMA, T. 2017 Streamwise vortex breakdown in supersonic flows. *Phys. Fluids* **29**, 054102.
HIEJIMA, T. 2018 Onset conditions for vortex breakdown in supersonic flows. *J. Fluid Mech.* **840**, R1.
HIEJIMA, T. 2019 Compressibility effects of supersonic Batchelor vortices. *Phys. Rev.* F **4**, 093903.
HOLM, D. D. & KERR, R. M. 2007 Helicity in the formation of turbulence. *Phys. Fluids* **19** (2), 025101.
JACQUIN, L. & PANTANO, C. 2002 On the persistence of trailing vortices. *J. Fluid Mech.* **471**, 159–168.
JAMESON, A., SCHMIDT, W. & TURKEL, E. 1981 Numerical simulation of the Euler equations by finite volume method using Runge–Kutta time stepping schemes. *AIAA Paper* 81–1259.
JEONG, J. & HUSSAIN, F. 1995 On the identification of a vortex. *J. Fluid Mech.* **285**, 69–94.
JOLY, L., FONTANE, J. & CHASSAING, P. 2005 The Rayleigh–Taylor instability of two-dimensional high-density vortices. *J. Fluid Mech.* **537**, 415–431.
KALKHORAN, I. M., SMART, M. K. & WANG, F. Y. 1998 Supersonic vortex breakdown during vortex/cylinder interaction. *J. Fluid Mech.* **369**, 351–380.
KHORRAMI, M. & CHANG, C. 1997 Linear and nonlinear evolution of disturbances in supersonic streamwise vortices. *AFOSR–TR*–97.
KHORRAMI, M. R. 1991 On the viscous modes of instability of a trailing line vortex. *J. Fluid Mech.* **225**, 97–212.
LEBLANC, S. & LE DUC, A. 2005 The unstable spectrum of swirling gas flows. *J. Fluid Mech.* **537**, 433–442.
LEIBOVICH, S. & STEWARTSON, K. 1983 A sufficient condition for the instability of columnar vortices. *J. Fluid Mech.* **126**, 335–356.
LELE, S. K. 1994 Compressibility effects on turbulence. *Annu. Rev. Fluid Mech.* **26**, 211–254.
LESSEN, M. & PAILLET, F. 1974 The stability of a trailing line vortex. Part 2. Viscous theory. *J. Fluid Mech.* **65**, 769–779.
LESSEN, M., SINGH, P. J. & PAILLET, F. 1974 The stability of a trailing line vortex. Part 1. Inviscid theory. *J. Fluid Mech.* **63**, 753–763.
MAO, X. & SHERWIN, S. J. 2012 Transient growth associated with continuous spectra of the Batchelor vortex. *J. Fluid Mech.* **697**, 35–59.
MAYER, E. W. & POWELL, K. G. 1992 Viscous and inviscid instabilities of a trailing vortex. *J. Fluid Mech.* **245**, 91–114.
MOFFATT, H. K. 2017 Helicity-invariant even in a viscous fluid. *Science* **357** (6350), 448–449.
MOFFATT, H. K. & TSINOBER, A. 1992 Helicity in laminar and turbulent flow. *Annu. Rev. Fluid Mech.* **24** (1), 281–312.
MORKOVIN, M. V. 1992 Mach number effects on free and wall turbulent structures in light of instability flow interactions. In *Studies in Turbulence* (ed. S. S. T. B. Gatski & C. G. Speziale), pp. 269–284. Springer.
NAUGHTON, J. W., CATTAFESTA, L. N. & SETTLES, G. S. 1997 An experimental study of compressible turbulent mixing enhancement in swirling jets. *J. Fluid Mech.* **330**, 271–305.
NONOMURA, T. & FUJII, K. 2013 Robust explicit formulation of weighted compact nonlinear scheme. *Comput. Fluids* **85** (suppl. C), 8–18.
OLENDRARU, C., SELLIER, A., ROSSI, M. & HUERRE, P. 1999 Inviscid instability of the Batchelor vortex: absolute-convective transition and spatial branches. *Phys. Fluids* **11**, 1805–1820.
PAPAMOSCHOU, D. & ROSHKO, A. 1988 The compressible turbulent shear layer experimental study. *J. Fluid Mech.* **197**, 453–477.
PARRAS, L. & FERNANDEZ-FERIA, R. 2007 Spatial stability and the onset of absolute instability of Batchelor's vortex for high swirl numbers. *J. Fluid Mech.* **583**, 27–43.
POUQUET, A. & MININNI, P. D. 2010 The interplay between helicity and rotation in turbulence: implications for scaling laws and small-scale dynamics. *Phil. Trans. R. Soc. Lond.* **368** (1916), 1635–1662.
QADRI, U. A., MISTRY, D. & JUNIPER, M. P. 2013 Structural sensitivity of spiral vortex breakdown. *J. Fluid Mech.* **720**, 558–581.

https://doi.org/10.1017/jfm.2020.388 Published online by Cambridge University Press

RAGAB, S. & SREEDHAR, M. 1995 Numerical simulation of vortices with axial velocity deficits. *Phys. Fluids* **7**, 549–558.

RAYLEIGH, LORD 1917 On the dynamics of revolving fluids. *Proc. R. Soc. Lond.* A **93** (648), 148–154.

SAHOO, G., BONACCORSO, F. & BIFERALE, L. 2015 Role of helicity for large-and small-scale turbulent fluctuations. *Phys. Rev.* E **92** (5), 051002.

SCHMID, P. J. & HENNINGSON, D. S. 2001 *Stability and Transition in Shear Flows*. Springer.

SIPP, D., FABRE, D., MICHELIN, S. & JACQUIN, L. 2005 Stability of a vortex with a heavy core. *J. Fluid Mech.* **526**, 67–76.

STEWARTSON, K. & BROWN, S. N. 1985 Near-neutral centre-modes as inviscid perturbations to a trailing line vortex. *J. Fluid Mech.* **156**, 387–399.

STOTT, J. A. K. & DUCK, P. W. 1994 The stability of a trailing-line vortex in compressible flow. *J. Fluid Mech.* **269**, 323–351.

UBEROI, M. S. 1979 Mechanisms of decay of laminar and turbulent vortices. *J. Fluid Mech.* **90** (2), 241–255.

VIOLA, F., ARRATIA, C. & GALLAIRE, F. 2016 Mode selection in trailing vortices: harmonic response of the non-parallel Batchelor vortex. *J. Fluid Mech.* **790**, 523–552.

WADA, Y. & LIOU, M.-S. 1994 A flux splitting scheme with high-resolution and robustness for discontinues. *AIAA Paper* 94–0083.

WANG, F. Y. & SFORZA, P. M. 1997 Near-field experiments on tip vortices at Mach 3.1. *AIAA J.* **35** (4), 750–753.

https://doi.org/10.1017/jfm.2020.388 Published online by Cambridge University Press